

# Local Structure of Well-Ordered Crystals and Systems with Competing Interactions

## Chapter Outline

- |  |            |   |            |
|--|------------|---|------------|
| <b>8.1. Structure of Well-Ordered Crystals</b>                               | <b>326</b> | Magnetoresistance in the Manganites   | <b>349</b> |
| 8.1.1. PDF of Ideal and Distorted Perovskites                                | <b>326</b> | <b>8.4. Local Correlations and Phase Transitions</b>  | <b>351</b> |
| 8.1.2. Complex Periodic Structure: AFE Lead Zirconate                        | <b>333</b> | 8.4.1. Phase Transitions in Complex Materials   | <b>354</b> |
| 8.1.3. Negative Thermal Expansion Materials                                  | <b>338</b> | 8.4.2. Phase Transitions in Systems with Competing Interactions I: Relaxor Ferroelectricity | <b>357</b> |
| <b>8.2. Quasicrystals</b>  | <b>342</b> | 8.4.3. Mechanism of Relaxor Ferroelectricity  | <b>359</b> |
| <b>8.3. Competing Interactions in Complex Oxides</b>                         | <b>343</b> | <b>8.5. Phase Transition in Systems with Competing Interaction: Lithium-Nickelate</b>       | <b>363</b> |
| 8.3.1. PZT, $\text{Pb}(\text{Zr}_{1-x}\text{Ti}_x)\text{O}_3$                | <b>345</b> | 8.5.1. Hidden Phase Transition and Local Structure in $\text{LiNiO}_2$                      | <b>364</b> |
| 8.3.2. Relaxor FE PMN, $\text{Pb}(\text{Mg}_{1/3}\text{Nb}_{2/3})\text{O}_3$ | <b>347</b> | 8.5.2. Domain Formation in $\text{LiNiO}_2$   | <b>364</b> |
| 8.3.3. Charge Ordering, Nanophase Separation, and Colossal                   |            |   |            |

## 8.1. STRUCTURE OF WELL-ORDERED CRYSTALS

Now that the reader is familiar with the PDF method, in the following several chapters we show examples for which the PDF approach contributed greatly to the understanding of the structure that is either complex, disordered, or both. We start the relatively simple case of well-ordered structure and proceed to more complex structures.

### 8.1.1. PDF of Ideal and Distorted Perovskites

Perovskite,  $\text{ABO}_3$ , is one of the most common oxide structures. In the ideal state, it has a cubic unit cell, with an A-site at the center of the cube, B-sites at the corners, and oxygen ions at the edge centers. Equivalently, we can place a B-site ion at the center of the cube, A-site ions at corners, and oxygen ions at the face-centers (Fig. 8.1). The B-site ion is characterized as having six oxygen nearest neighbors and residing in a  $\text{BO}_6$  octahedron (Fig. 8.2a). The A-site ion has 12 oxygen neighbors (Fig. 8.2b). A very large number of oxide compounds have a structure that is a derivative of perovskite. In the ideal cubic structure, the A—O and O—O bonds have to be equal in length and have to be  $\sqrt{2}$  times longer than the B—O bond that is the shortest bond. However, only in exceptional cases do the bond lengths have such a ratio. If the ratio between the A—O and B—O bond lengths is not equal to  $\sqrt{2}$ , an

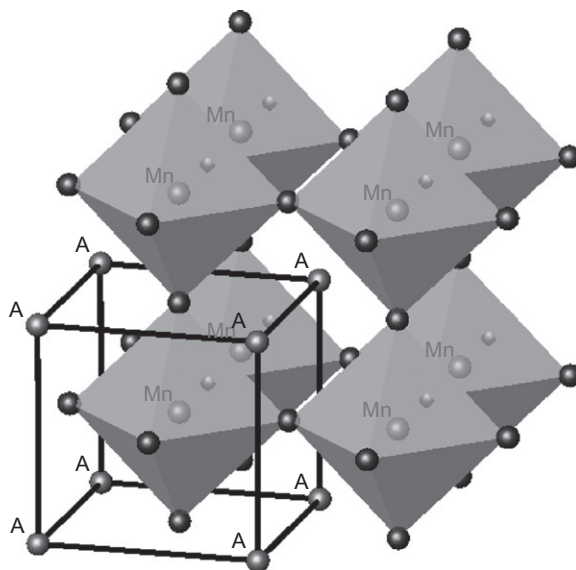


**FIGURE 8.1** Picture of the perovskite structure. B-site ions (in this case Mn indicated in red) sit at the center of oxygen (blue) octahedra. The A-site (green) resides in the cavities made by the network of octahedra.

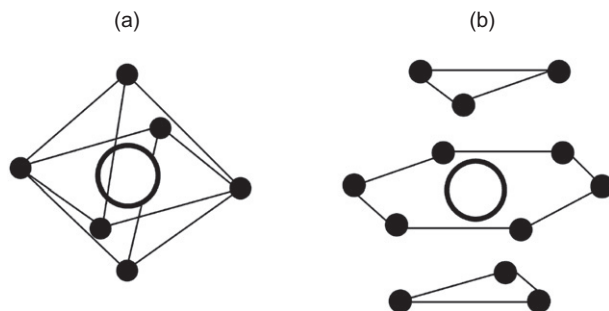


**FIGURE 8.2** Coordination of the A- and B-site ions shown more explicitly. (a)  $\text{BO}_6$  octahedron, (b)  $\text{AO}_{12}$  cluster.

ideal perovskite cannot be formed, and the structure becomes distorted. It is customary to express this balance in terms of the tolerance factor,  $t = \frac{R_{\text{A-O}}}{\sqrt{2}R_{\text{B-O}}}$ . The bond length between two ions is, to a good approximation, the sum of their “ionic radii,” which is empirically specified for given valence and coordination (Shannon and Prewitt, 1969; Shannon, 1976). Thus, in order to satisfy the condition for the ideal perovskite structure, the ionic radius of the A ion has to be equal to that of oxygen ( $R_{\text{O}} = 1.40 \text{ \AA}$ ), and the radius of the B ion has to be  $(\sqrt{2} - 1)R_{\text{O}} = 0.58 \text{ \AA}$ . This condition strongly limits the choice of ions, so that almost all perovskite compounds have a distorted structure. When  $t$  is less than unity, most commonly the  $\text{BO}_6$  octahedra become tilted, often around the  $[111]$  axis, and the structure becomes rhombohedral.

As we see below, the  $\text{BO}_6$  octahedron tends to behave as a unit, and its rotation or tilting is often a key to define the structure. A detailed analysis of the different classes and space-groups of octahedrally tilted perovskite structures has been given by Woodward (1997a,b). For instance, tilting of a  $\text{BO}_6$  octahedron induces tilting of the adjacent  $\text{BO}_6$  octahedron in the opposite sense resulting in a doubling of the unit cell. This often results in antiferroelectric (AFE) or ferroelastic behavior. On the other hand, if  $t$  is greater than unity, the  $\text{BO}_6$  octahedron will be distorted, becoming usually elongated. Some of the B-site ions, such as  $\text{Ti}^{4+}$  or  $\text{W}^{6+}$ , have a tendency to become off-centered, resulting in ferroelectricity. In addition, some A-site ions, such as  $\text{Pb}^{2+}$  or  $\text{Li}^+$ , prefer directional bonding with oxygen ions, and an asymmetric A-site environment, enhancing the ferroelectric (FE) polarization (e.g., see Cohen, 1992). In this way, the ionic size has a direct consequence on the properties of the compounds. A major goal of solid-state chemistry is to understand these structure–property relationships in the quest to design new compounds.

$\text{SrTiO}_3$  (STO) is a prototypical perovskite with the ideal perovskite structure at room temperature. Indeed, the tolerance factor of STO is very close to unity ( $t = 1.02$ ). Below 110 K, however, the structure deviates very slightly from cubic and becomes rhombohedral. The PDF of STO determined by

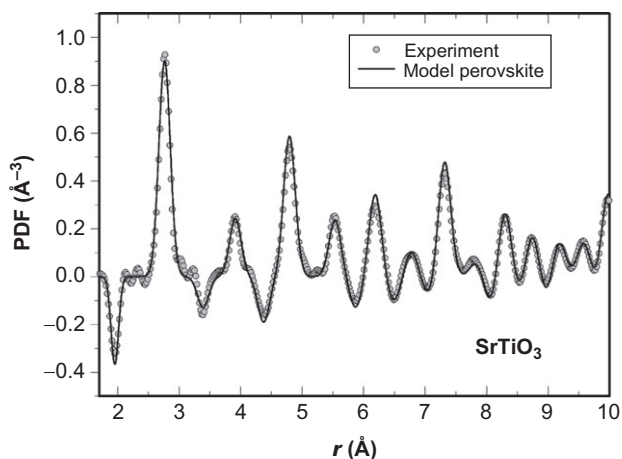


**FIGURE 8.3** Pulsed neutron PDF of  $\text{SrTiO}_3$  at  $T = 10$  K (Louca and Egami, 1999).

pulsed neutron scattering at  $T = 10$  K is shown in Fig. 8.3 (Louca and Egami, 1999). The PDF shown in Fig. 8.3 has a negative first peak. This is because the neutron scattering length,  $b$ , is negative for Ti and positive for O so, as a result of Eq. 3.5, the Ti–O peak appears negative. The PDF compares very well with the calculated PDF with the thermal amplitude of  $0.07$  Å. The magnitude of the thermal factor is consistent with the Debye temperature of this solid. The distances and the coordination numbers obtained by integrating the RDF over the peak are shown in Table 8.1 and agree well with the values expected for the structure. Since the peaks start to overlap beyond the second peak and positive and negative peaks cancel each other, the coordination number of high order peaks cannot be determined by direct integration. However, agreement of the PDF with the model PDF indicates that the PDF is accurate over the range shown.

$\text{BaTiO}_3$  is another prototypical FE perovskite and is one of the most heavily studied materials (Kwei *et al.*, 1993 and references therein). At high temperature, it has a centrosymmetric cubic structure, but on cooling, it undergoes a series of distortive phase transitions into FE phases with the FE polarization vector along  $[001]$  (below 393 K, tetragonal),  $[011]$  (below 278 K, orthorhombic), and  $[111]$  (below 183 K, rhombohedral). These distortions are shown schematically in Fig. 8.4. A long-standing controversy existed about the structure of this material that is highly pertinent to the discussions of this book. In each of the distorted phases, crystallography revealed small atomic displacements of Ti and O along the directions of the polarization vectors (Kwei *et al.*, 1993). On the other hand, X-ray diffuse scattering (total scattering) measurements indicated that the atomic displacements of Ti were always along  $[111]$  directions corresponding to the eight faces of the  $\text{TiO}_6$  octahedra (Comes *et al.*, 1968, 1970). As the sample

**TABLE 8.1** Peak Positions and Number of First and Second Neighbors in SrTiO<sub>3</sub> Expected from the Crystal Structure and Measured Directly (in a Model-Independent Way) from the PDF

Compound	Coordination shell	Peak position (Å)		Number of neighbors	
		Expected	Measured	Expected	Measured
SrTiO <sub>3</sub>	First (Ti–O)	1.95	1.95	6	5.97
	Second (O–O, Sr–O)	2.77	2.77	36	36.87

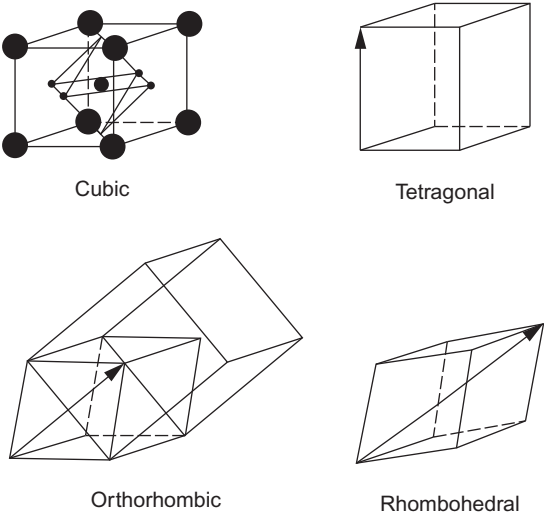


**FIGURE 8.4** Schematic diagrams of the distortive phase transitions in BaTiO<sub>3</sub> on lowering temperature. The arrow indicates the direction along which the cubic unit cell is distorted and also the direction of the ferroelectric polarization. The larger unit-cell superimposed in the orthorhombic case shows the relationship of the crystallographic orthorhombic unit cell to the distorted pseudo-cubic cell (Kwei *et al.*, 1993).

changed temperature, the relative occupancies of the different displaced sites changed. Thus, in the low-temperature rhombohedral phase, only one of the eight displaced sites was preferred, in the orthorhombic variant, two out of the eight, in the tetragonal variant, four of the eight, and in the high-temperature cubic, all eight are equally populated (presumably dynamically). This result was somewhat controversial because BaTiO<sub>3</sub> was considered to be an archetypal phonon soft-mode material where the distortive phase

transitions happened by the condensation of an unstable phonon mode (Jona and Shirane, 1962), and this is a clear example of the above discussion where PDF and soft-mode theory are apparently at odds. The local structural measurements that indicated a significant order–disorder component to the phase transition tended to muddy this elegant and simple soft-mode picture. PDF measurements of these materials tend to support the Comes *et al.* (1968, 1970) picture at the local level since changes in the local structure at these phase transitions are very small (Kwei *et al.*, 1995) as shown in Fig. 8.5. This result can be understood if atomic displacements (to which the PDF is

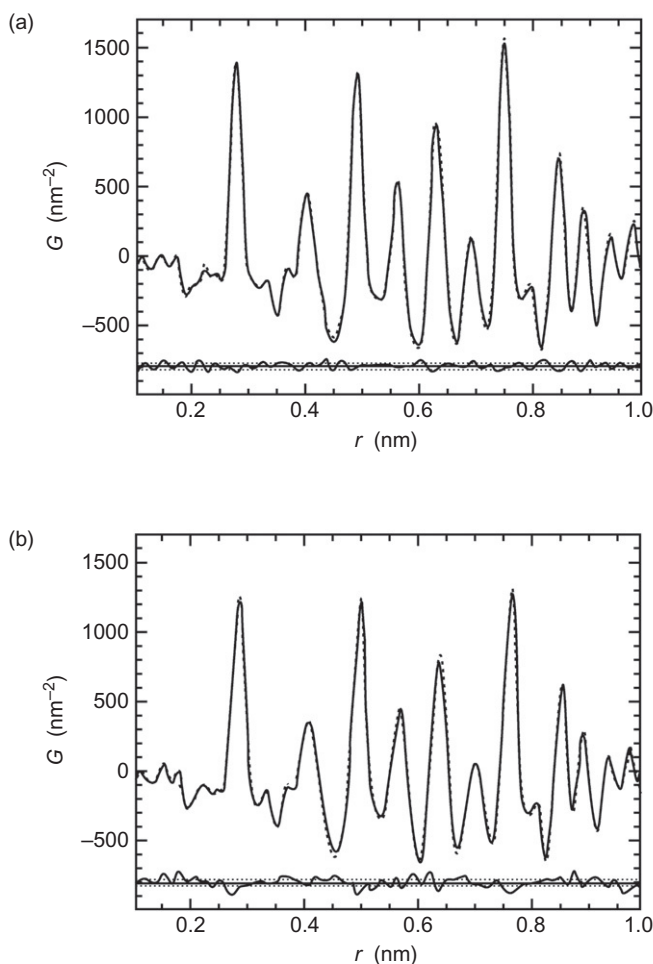


**FIGURE 8.5** PDFs of  $\text{BaTiO}_3$  on passing through the (a) rhombohedral to orthorhombic and (b) orthorhombic to tetragonal phase transitions shown in Fig. 8.4. Data above (b) the transition are solid (dashed) lines. A difference curve is shown below the data. Changes in the local structure are very small at these transitions (Kwei *et al.*, 1995).

rather sensitive) are not changing significantly but ordering between the displaced sites (to which the PDF is rather insensitive) is changing.

PbTiO<sub>3</sub> (PT) is cubic at high temperatures, but it becomes FE below  $T_c$  and the structure distorts to tetragonal. The ionic radius of Pb<sup>2+</sup> is 1.49 Å and that of Ti<sup>4+</sup> is 0.605 Å. Thus, the tolerance factor is equal to 1.019. However, in this case, the tolerance factor is less important in determining the crystal structure. What is most important is the asymmetry of the atomic bonds for both Pb and Ti. Pb<sup>2+</sup> has the electron configuration of (Xe) (4f)<sup>14</sup>(6d)<sup>10</sup>(6s)<sup>2</sup>, and the two s electrons tend to form directional bonds by hybridizing with the oxygen p-orbitals. Consequently, Pb<sup>2+</sup> becomes off-centered in the oxygen cage of PbO<sub>12</sub> resulting in shorter and longer Pb–O bonds of 2.54, 2.8, and 3.2 Å. Ti<sup>4+</sup>, on the other hand, is ferroelectrically active and tends also to become off-centered in the TiO<sub>6</sub> octahedra with bonds of 1.78, 1.97, and 2.37 Å. As a result of these off-centering tendencies, PT becomes strongly FE, with a tetragonal distortion. The bond distances determined from the PDF and those from the crystallographic structure show good agreement (Dmowski *et al.*, 2002). The PDF method is an excellent technique to study ferroelectricity. Local polarization produces different metal–oxygen bond distances that induce the splitting of the metal–oxygen PDF peak. As shown in Fig. 8.6 (Kwei *et al.*, 1995), at low temperatures, the three kinds of Ti–O bonds are clearly evident, while in an ideal perovskite structure (Fig. 8.1), there is only one distance between a B-site metal and its closest oxygen. The splitting of the Ti–O distance in Fig. 8.6 indicates a strong FE polarization of Ti in the TiO<sub>6</sub> octahedron. If we take Ti as the origin, at low temperatures, Pb is displaced from the ideal position by 0.2 Å along the *c*-axis and oxygen by 0.3 Å in the opposite direction. Thus, both Ti and Pb are strongly off-centered within the oxygen cage and contribute to the FE dipolar moment.

Another example of a distorted perovskite is the Jahn–Teller (JT) distorted compound LaMnO<sub>3</sub>. The tolerance factor of this compound is 0.986, and as a consequence, MnO<sub>6</sub> octahedra are rotated around the [111] axis. However, what makes this compound interesting is a further distortion due to the JT effect. LaMnO<sub>3</sub> provided a nice example from a well-ordered crystal where structural parameters determined from the PDF and using Rietveld refinement of the same powder diffraction data could be compared (Proffen *et al.*, 1999). The measured PDF and the best-fit model are shown in Fig. 1.8 with a difference curve underneath. Clearly, the agreement between Rietveld and PDF refined atomic positional parameters is excellent indicating that the PDF yields quantitatively accurate atomic positions when fit with an adequate model.

In LaMnO<sub>3</sub>, Mn is trivalent and has four d-electrons. The nearly cubic crystal-field splits the d-level into t<sub>2g</sub> (triplet) and e<sub>g</sub> (doublet) levels. The exchange coupling among the d-electrons (Hund coupling) is stronger than the crystal-field splitting, so that these d-electrons are fully spin polarized

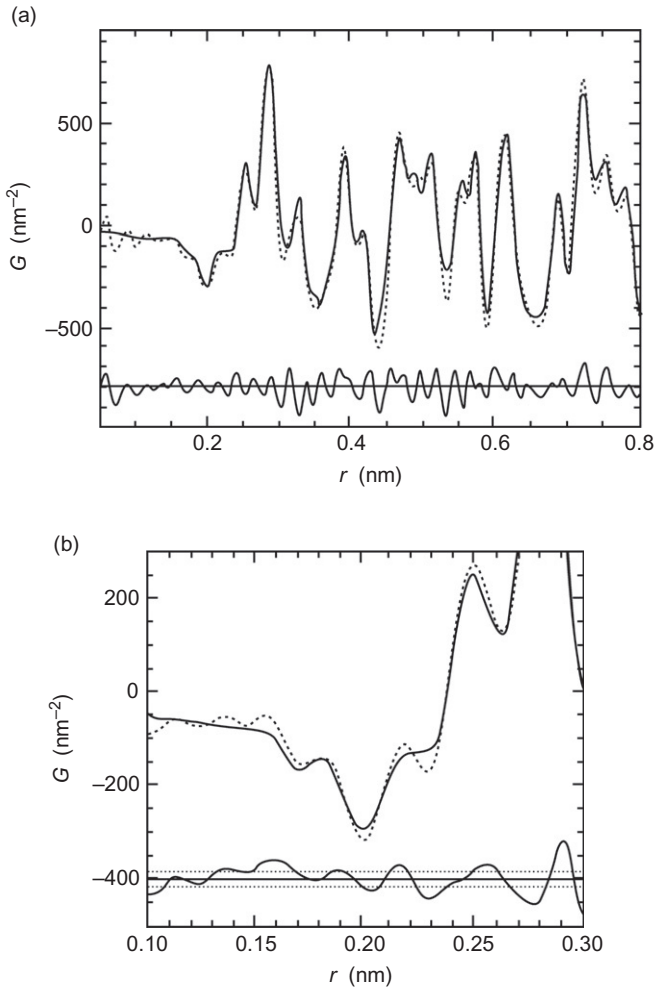


**FIGURE 8.6** (a) Pulsed neutron PDFs of  $\text{PbTiO}_3$  at  $T = 10$  K. Solid line is a model calculation using the tetragonal structure, dashed line indicates the data. A difference curve is shown below the data. (b) The PDF on an expanded scale to emphasize the near-neighbor Ti-O atom pairs. The vertical lines indicate the lengths of the six Ti-O bonds in a 1-4-1 configuration (Kwei *et al.*, 1995).

(the high-spin state). Thus, the majority spin  $t_{2g}$  level is filled and the  $e_g$  orbital is singly occupied. The  $e_g$  level is further split into two by a JT distortion that elongates the  $\text{MnO}_6$  octahedra (Fig. 1.8; Proffen *et al.*, 1999). As a result of the JT distortion, the Mn-O bond distances are grouped into four short (1.92 and 1.97 Å) and two long (2.16 Å) bonds (Proffen *et al.*, 1999).  $\text{LaMnO}_3$  has the orthorhombic ( $Pnma$ ) structure (Mitchell *et al.*, 1996; Lebedev *et al.*, 1998; Rodriguez-Carvajal *et al.*, 1998; Proffen *et al.*, 1999; Louca *et al.*, 2000). In this structure, the JT distortion is oriented in the  $a$ - $b$



plane with alternating directions (antiferromagnetic orbital ordering). With an excess of oxygen that creates vacancies at the cation sites, the structure changes to rhombohedral ( $R3C$ ) symmetry in which all six Mn—O bonds are equal in length.

## 8.1.2. Complex Periodic Structure: AFE Lead Zirconate

### 8.1.2.1. Low-Temperature Phase

Lead zirconate ( $\text{PbZrO}_3$ , PZ) is an end member of the family of a well-known FE oxide solid solution,  $\text{PbZr}_{1-x}\text{Ti}_x\text{O}_3$  (PZT). PZT is used as a FE or piezoelectric material in a wide variety of technological applications. Nevertheless, there have been raging controversies regarding the dielectric properties and atomic structure of PZ. The tolerance factor is equal to 0.973, so that  $\text{ZrO}_6$  octahedra are expected to be tilted or rotated. In addition, the polarizability of Pb, as discussed above, is expected to contribute to the distortion. Indeed, its structure is based upon the distorted and tilted perovskite but is rather complex with eight perovskite units forming the unit-cell structure containing 40 atoms. Two different symmetries have been proposed: noncentrosymmetric (FE)  $Pba2$  (Jona *et al.*, 1951) and centrosymmetric (AFE)  $Pbam$  (Fujishita *et al.*, 1982). A total electron energy calculation using the local density approximation demonstrated the coexistence of both FE and AFE instabilities in PZ, with a very delicate balance between them (Singh, 1995). In addition, there is a possibility of a second high-temperature phase with an unknown structure and ordering over a narrow temperature range near 510 K.

A powder pulsed neutron diffraction measurement was carried out at various temperatures, and the results were analyzed using both the Rietveld refinement method and the PDF analysis (Teslic and Egami, 1998). The neutron diffraction data were obtained using the Special Environment Powder Diffractometer at the IPNS. The sample, weighing 14.5 g, was sealed in a vanadium sample holder with He-exchange gas and cooled using a closed-loop He refrigerator for the low-temperature measurements. For the high-temperature measurements, the sample was sealed in a vanadium holder and heated using a vanadium furnace, and data were collected up to 523 K. The duration of each run was approximately 4 h per temperature point. Diffraction intensities were first analyzed by the Rietveld method using the IPNS Rietveld package over the  $d$  range of 0.5–4.0 Å with the resolution of  $\Delta d/d=0.006$ . The overall scale factor, parameters defining peak shapes, counter-zero error, atomic position parameters, isotropic thermal (atomic displacement) factors, and unit-cell parameters were refined. The PDF was calculated using the data of  $S(Q)$  up to  $35 \text{ \AA}^{-1}$ , with small damping for  $S(Q)-1$  between 30 and  $35 \text{ \AA}^{-1}$ .

The Rietveld analysis suggested that the symmetry of PZ at  $T=20 \text{ K}$  is not the noncentrosymmetric  $Pba2$ , but the centrosymmetric  $Pbam$ . The PDF

calculated from the Rietveld-refined model showed excellent agreement with the PDF data as shown in Fig. 6.5. Real-space refinement over the range of  $1.8 \leq r \leq 0.5 \text{ \AA}$  produced an almost identical result. Thus, the Rietveld method and the PDF method are in full agreement with the structure of PZ at 20 K. Note that, in the PDF analysis, just 28 parameters were refined including position and thermal parameters and the  $S(Q)$  normalization factor, while in the crystallographic refinement, 27 structural parameters were refined in *Pbam* symmetry in addition to 9 parameters which include the scale factor, background parameters as well as extinction and absorption parameters. The maximum allowed number of independent parameters in this real-space range is 80 (Billinge, 1992), more than twice as many as were refined. The best-fit model in the real-space refinement gave an *A*-factor of 7.87% with e.s.d. (*A*) = 0.12% over the range  $1.8 \leq r \leq 0.5 \text{ \AA}$ . Over this range,  $A_{\min}$  was 2.15% and, therefore, the goodness of fit (GoF) value is 3.66. This value is comparable to the GoF value of 3.20 attained in the Rietveld refinement of the same data. The only significant difference between the Rietveld-refined model and the real-space refined model was found in the value of the thermal (DW) factor of the equatorial oxygen O<sub>2</sub>. The Rietveld-refined thermal factor ( $B = 0.42 \text{ \AA}^2$ ) corresponds to an unreasonably high mean-square displacement,  $\langle u^2 \rangle$ , of  $5 \times 10^{-3} \text{ \AA}^2$ , while the PDF-refined value is  $1.5 \times 10^{-3} \text{ \AA}^2$ . The value of  $\langle u^2 \rangle$  calculated by the Einstein model is  $2.07 \times 10^{-3} \text{ \AA}^2$  for O, much closer to the value obtained by the PDF analysis.

In order to compare the refined variables in the Rietveld and PDF analyses, it is important to estimate their accuracy. This is possible by considering the uncertainties in the *A* and  $R_w$  factors and their best-fit curves as functions of a refined parameter. Then, the uncertainty in the refined parameter is given by the range of values for this parameter for which the *A* or  $R_w$  factors change by less than their e.s.d. The e.s.d. for the *A*-factor calculated by the propagation of e.s.d. of the data is  $\pm 0.12\%$ , which when calculated in this way results in uncertainties in O2(c), O3(c), and O4(c) parameters in the PDF analysis of  $\pm 0.01$ ,  $\pm 0.02$ , and  $\pm 0.02 \text{ \AA}$ . Similarly, the e.s.d. of the  $R_w$  factor is  $\pm 0.08\%$  and the uncertainties for O2(c), O3(c), and O4(c) were found to be  $\pm 0.07$ ,  $\pm 0.02$ , and  $\pm 0.04 \text{ \AA}$ , respectively, in the Rietveld analysis. Thus, the uncertainties in these position parameters in the PDF analysis are significantly smaller than those in the Rietveld analysis. Consequently, the atomic positions refined by the PDF analysis are most likely to be more accurate.

### 8.1.2.2. High-Temperature Phases

#### 8.1.2.2.1. Temperature Dependence

The crystal structure determined by the Rietveld analysis evolved smoothly and slowly with temperature. On the contrary, the PDF shows appreciable temperature dependence as shown in Fig. 8.7. In particular, the changes in

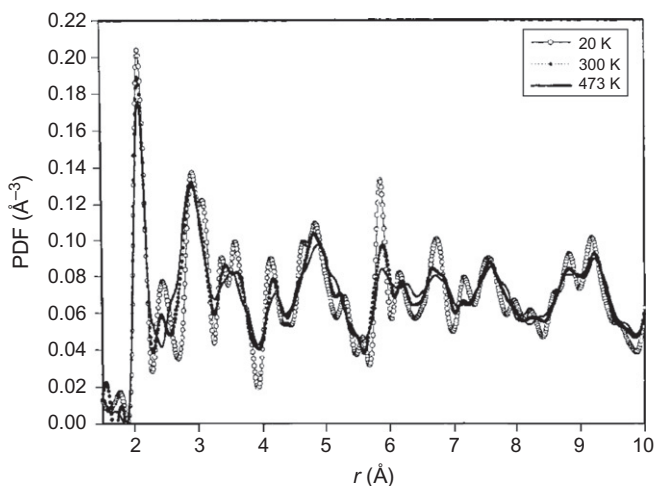


**FIGURE 8.7** Variation of the neutron PDF of  $\text{PbZrO}_3$  with temperature (Teslic and Egami, 1998).

the peak heights with temperature are not uniform across  $r$ , some peaks becoming much more smeared at 300 K than at 20 K. An increase in the thermal vibrational amplitude can account for only a small part of this change. For instance, the dramatic decrease in the height of the PDF peak at 5.9 Å cannot be explained by thermal phonons. This implies the existence of displacive disorder developing with temperature. It was found that disordered oxygen displacements at the equatorial sites lead to an improved fit. Introducing disorder in the pattern of alternative O3, O4 displacements improved the fit, lowering the  $A$ -factor nearly 1%.

#### 8.1.2.2.2. Anharmonic Displacements

The Rietveld-refined value for the thermal (DW) factor on the Pb site was anomalously large even at  $T = 20$  K. The reason is probably the presence of some disordered static or quasistatic displacive disorder on the Pb site along the  $c$ -axis leading to a large uncertainty in the atom position. In order to characterize such Pb displacements, the weighted Rietveld reliability factor  $R_w$  was evaluated as a function of the Pb displacement. To allow for such displacements, the refinement was carried out in the noncentrosymmetric  $Pba2$  space-group keeping the oxygen positions unchanged. The best-fit  $R_w$  factor as a function of a static displacement of Pb in the  $c$ -direction,  $\text{FE Pb}_c$ , is shown in Fig. 8.8.

A similar analysis with the PDF real-space method yielded a set of curves for the  $A$ -factor that shows minima more clearly than the Rietveld-derived results. Thus, we can conclude that a small static or quasistatic local FE Pb displacement in the  $c$ -direction develops. Using the PDF analysis, we can also detect the existence of correlation among  $\text{Pb}_c$  displacements and its range.

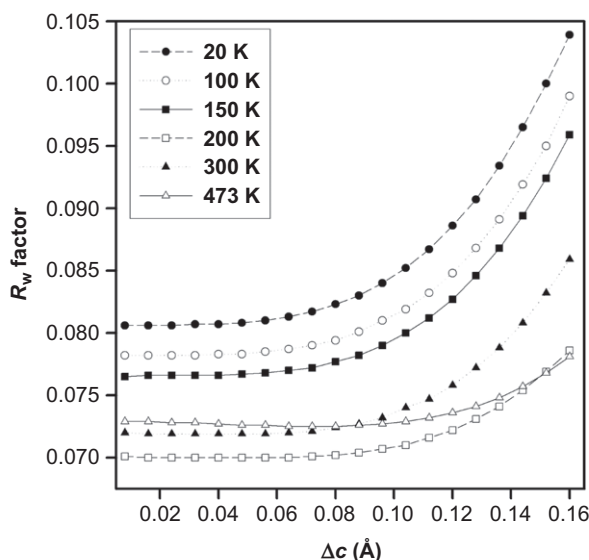


**FIGURE 8.8** The best-fit Rietveld  $R_w$  factor as a function of Pb displacement along the  $c$ -axis in  $\text{PbZrO}_3$  (Teslic and Egami, 1998).

Keeping fixed the magnitude of the  $\text{Pb}_c$  displacement that produced the best-fit model in the range 1.8–9.5 Å, the PDFs with FE and random  $\text{Pb}_c$  displacements for interatomic distances up to 40 Å were compared. It was found that the FE correlation length at low temperatures was estimated to be about 10 Å. For this reason, we conjecture that the  $\text{Pb}_c$  displacements must be quasistatic rather than static.

At 473 K, both the reciprocal- and real-space refinements indicated a FE displacement of Pb in the  $c$ -direction. The best-fit curve for the  $R_w$  factor shows shallow minima at  $\pm 0.08$  Å. In the PDF refinement, the  $A$ -factor curve has somewhat deeper minima at  $\pm 0.14$  Å before finally diverging at a larger value of  $\Delta = 0.20$  Å, as shown in Fig. 8.9. It was found that the  $\text{Pb}_c$  correlation length to be about 20 Å at this temperature.

#### 8.1.2.2.3. Intermediate Phase

The Rietveld analysis for the intermediate phase turned out to be extremely difficult, yielding large  $R_w$  factors and thermal factors. The structure apparently is not correctly described by either the  $Pbam$  or  $Pba2$  symmetry phases. The PDF analysis also encountered great difficulties. However, a different, simpler AFE pattern with alternating Pb displacements within the  $ab$  plane (AFE-II, Fig. 8.10b), as opposed to the double row AFE pattern at low temperatures (AFE-I, Fig. 8.10a), was found to provide good agreement. This phase also has a large FE Pb displacement in the  $c$ -direction, and the

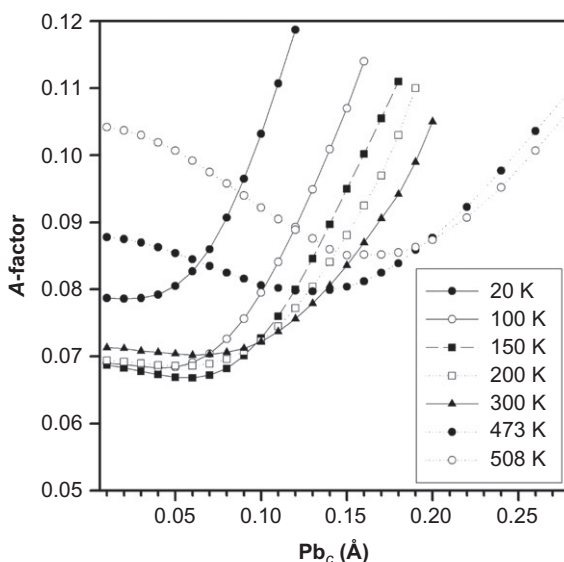


**FIGURE 8.9** The best-fit PDF A-factor as a function of Pb displacement along the  $c$ -axis in  $\text{PbZrO}_3$  (Teslic and Egami, 1998).

correlation extends up to  $30 \text{ \AA}$ , while it is inconclusive whether the FE long-range order is established.

#### 8.1.2.2.4. Paraelectric Phase

Although PZ at high temperatures (above 508 K) was crystallographically refined as cubic, very small differences were observed in the PDF between 508 and 523 K (Teslic and Egami, 1998). This implies that the PE phase is locally polarized, and that the FE phase transition has the order/disorder character (Stern and Yacoby, 1996). This point, however, requires further discussion developed in Chapter 11. The PDF refinement of the data at 523 K showed that Pb atoms were displaced along the  $[111]$  direction. The displacements are spatially correlated only over short range; therefore, they are not directly observable in the reciprocal-space analysis.

#### 8.1.2.3. Pb Polarization

As we discussed above,  $\text{Pb}^{2+}$  has two 6s electrons that are high in energy and readily hybridize with the oxygen p-orbitals, forming covalent bonds with 2–4 oxygen ions. Consequently, the  $\text{PbO}_{12}$  dodecahedral cluster becomes strongly off-centered as shown in Fig. 8.11. The center of gravity of the  $\text{O}_{12}$  cage is separated from the position of the Pb ion by as much as  $0.5 \text{ \AA}$ . This produces a strong local ionic polarization of the  $\text{PbO}_{12}$  cluster. The structure and structural transition in PZ can be understood in terms of interaction among these

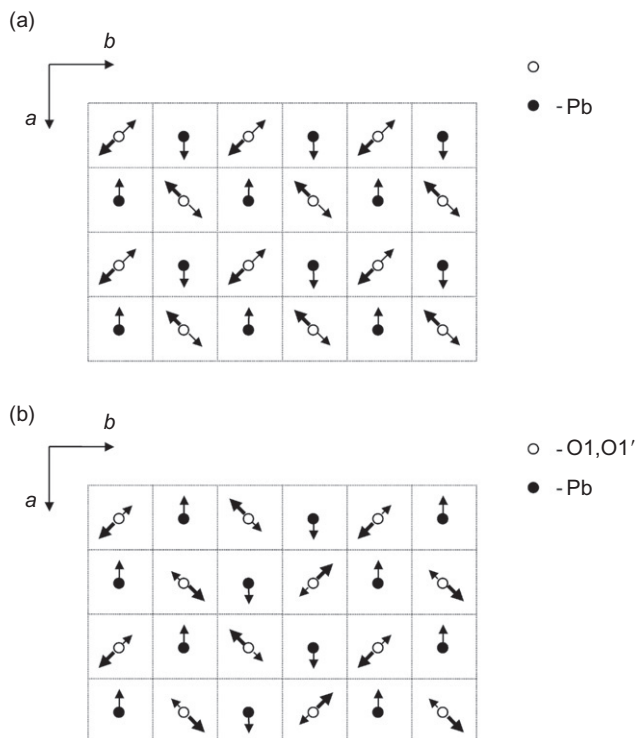


**FIGURE 8.10** (a) AFE pattern of atom displacements for the intermediate phase (AFE-II), (b) AFE pattern for the low-temperature phase (AFE-I). View is down the crystallographic  $c$ -axis. Solid circles indicate Pb and the open circles oxygen. The arrows indicate the directions of atomic displacement (Teslic and Egami, 1998).

local  $\text{PbO}_{12}$  polarizations and their reorientation as we will discuss in Chapter 10. In PT,  $\text{Pb}^{2+}$  is displaced in the  $[100]$  direction, forming covalent bonds with four oxygen ions. In PZ, the direction of the  $\text{Pb}^{2+}$  displacement is  $[110]$ , in the coordinates of the pseudo-cubic perovskite lattice, again with four close oxygen ions. In the average structure of rhombohedral PZT,  $\text{Pb}^{2+}$  is displaced in the  $[111]$  direction, but locally the direction is closer to  $[110]$  as discussed later. Thus,  $\text{Pb}^{2+}$  apparently prefers to be off-center either in  $[100]$  or  $[110]$  directions, but not in the  $[111]$  direction. This could be due to the partial involvement of the p-orbital in the covalent bond. This is very similar to the behavior seen in the covalent alloy  $\text{In}_{1-x}\text{Ga}_x\text{As}$  (Sections 1.2.1 and 9.2.1)

### 8.1.3. Negative Thermal Expansion Materials

Most materials expand on warming. Finding materials with zero or negative thermal expansion (NTE) is therefore of technological importance and scientific

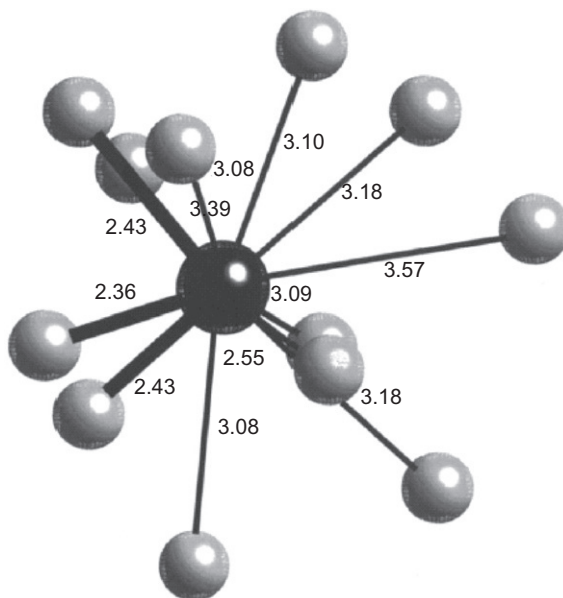


**FIGURE 8.11** Oxygen neighbors of Pb in  $\text{PbZrO}_3$  in the ferroelectric phase. Numbers indicate distances in Å (Teslic and Egami, 1998).

interest. By making composites of NTE and positive thermal expansion materials, it is possible to construct packaging for devices that have to survive operation in different temperature conditions. A number of network oxides show rather large and robust NTE and, apart from some tiny details, the mechanism is quite well worked out. The structure is a network of fairly rigid geometric units such as  $\text{MO}_4$  tetrahedra and  $\text{MO}_6$  octahedra, where M is a metal ion, which are linked by bridging oxygen atoms that provide flexible links or hinges. The motion of the oxygen bridging atoms is only weakly constrained, and the energy to excite large amplitude motions of these ions is small. At high temperatures, large amplitude oscillations of these oxygen linkers therefore occur, but they are rigidly joined to their neighboring metal ions through a strong covalent bond. The system responds by pulling the neighboring metal ions closer to one another. The larger the amplitude of oxygen vibrations the closer the metal centers get. This is illustrated schematically in Fig. 8.12. The PDF paid a large role in sorting out this behavior, beginning with work on silicates in the late 1990s. Similar effects are seen in the giant NTE material  $\text{ZrW}_2\text{O}_8$  (Tucker *et al.*, 2005), though there is disagreement about the exact nature of the rigid units involved (Cao *et al.*, 2002; Tucker *et al.*, 2005). The nice thing about the PDF is that it is possible to see these effects directly in a model-independent way. Whereas the crystallographically measured bond length shortens with increasing temperature, the PDF directly measures the local bond length and this is seen to lengthen over the same temperature range

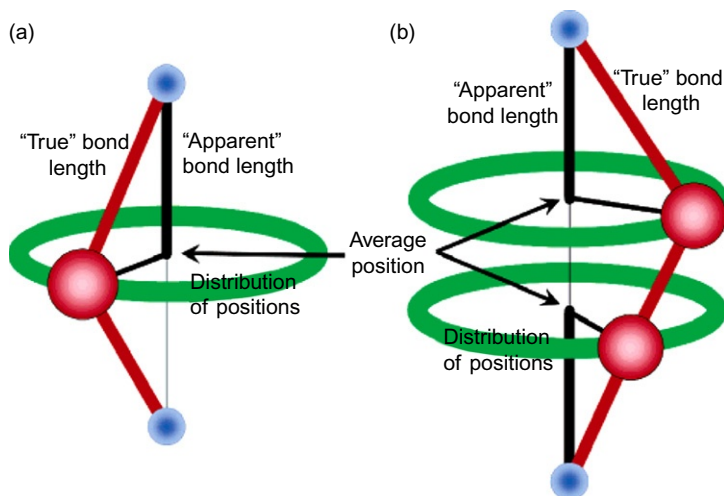


**FIGURE 8.12** Schematic illustration of the NTE mechanism in a covalent network material. As the amplitude of motion of the oxygen increases, the “true” bond length stays the same, or actually increases slightly, but the “apparent” bond length shortens. This effect is enhanced in cyanides because the bridging ions are not a single atom but a linear molecule (Chapman *et al.*, 2005).

(Tucker *et al.*, 2000, 2001a,b, 2002). This is shown in Fig. 8.13 for the cyanide material,  $\text{Zn}(\text{CN})_2$  (Chapman *et al.*, 2005) that is discussed below. The left panel shows bond lengths determined crystallographically, and the right panel shows the same bond lengths obtained directly from the PDF, plotted as a function of temperature. In each case, the bottom curve is the nearest-neighbor Zn—cyanide bond and the top curve is the next-neighbor Zn—C/N bond. The PDF data clearly show the nearest-neighbor bond lengthening on warming (regular thermal expansion due to anharmonic effects) even though, crystallographically, it appears to be shortening (left panel).

The zinc cyanide material mentioned above exhibits a very large NTE (Chapman *et al.*, 2005). The mechanism is roughly the same as for the oxides but the fact that the bridging oxygen is replaced by a bridging C—N molecule (Fig. 8.12) amplifies the effect. Another recently discovered related material,  $\text{Ag}_3[\text{Co}(\text{CN})_6]$  exhibits colossal NTE and positive thermal expansion effects (Goodwin *et al.*, 2008). This behavior was recently studied in great depth using total scattering and PDF methods (Conterio *et al.*, 2008) coupled with RMC analysis. These related studies are the book-ends of PDF analysis in some sense. On the one hand, confirmation of the mechanism of NTE in  $\text{Zn}(\text{CN})_2$  was obtained directly from a study of the temperature dependence of individual peaks in the PDF itself. On the other hand, sophisticated Big Box modeling was used to wring as much information as possible from the data to gain insight into the physics of the colossal NTE in the network material



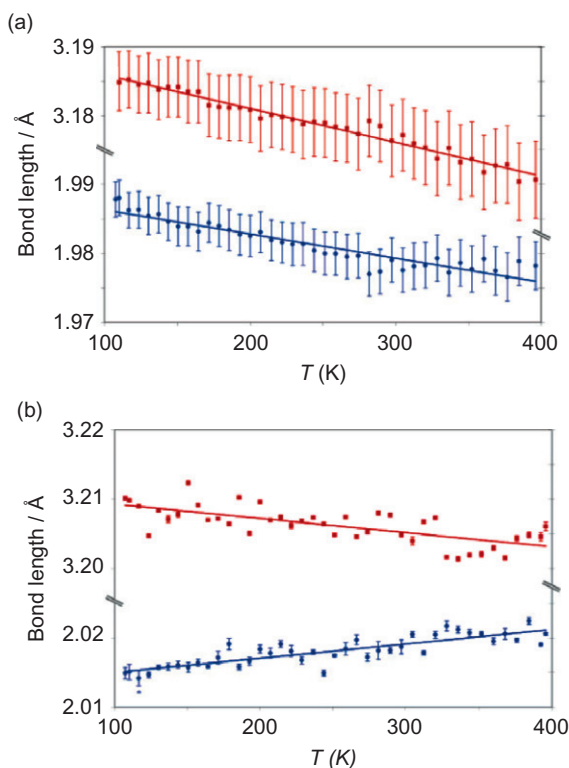


**FIGURE 8.13** Temperature evolution of the Zn–CN atom pair distances from  $\text{Zn}(\text{CN})_2$ . The bottom curves are the nearest-neighbor Zn–C/N bond and the top curve is the next-neighbor Zn–C/N distance. The left panel is the crystallographic result and the right panel is the PDF result. The Zn–C/N bond is lengthening with increasing temperature in the local structure, but on average, crystallographically, it is shortening (Chapman *et al.*, 2005).

$\text{Ag}_3[\text{Co}(\text{CN})_6]$ . In this latter study, a reverse Monte Carlo approach was used but with constraints provided not only by data but also using geometric algebra which constrained parts of the structure to move as rigid units. Phonon densities of states (PDOS) were obtained not by direct measurement but by sampling the RMC configurations directly. The origin of the phonon information in the PDF has been discussed in more detail in Chapters 6 and 7. Large changes in the PDOS are observed with temperature with a large overall softening of the spectrum. The Ag partial PDOS obtained from the RMC are shown in Fig. 8.14. Slightly surprisingly, at the time of writing, we are aware of no inelastic neutron scattering measurement that has been carried out to supplement this information. Nonetheless, this is an example of highly sophisticated modeling giving insight into the mechanism of interesting material properties.

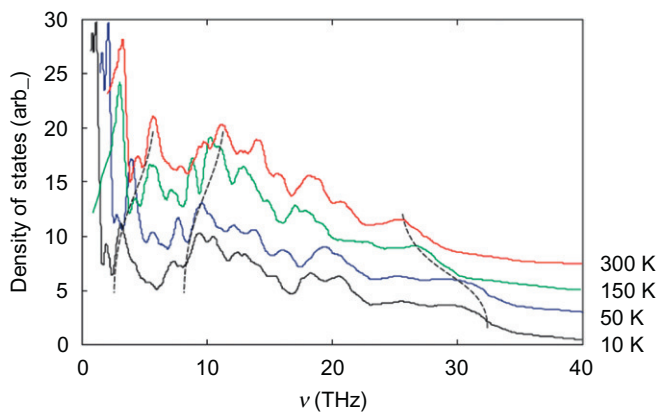


**FIGURE 8.14** The partial phonon density of states projected on the Ag ion, determined from RMC configurations that were fit to the total scattering data in  $\text{Ag}_3[\text{Co}(\text{CN})_6]$  (Conterio *et al.*, 2008).

## 8.2. QUASICRYSTALS

Quasicrystals were discovered by Dan Shechtman in 1982, for which he received the 2011 Nobel prize in chemistry (though it took 2 years to get his paper published) (Shechtman *et al.*, 1984). They are materials that have long-range orientational order but no translational symmetry. The most common quasicrystals have the icosahedral symmetry, and their diffraction patterns feature remarkable fivefold symmetry. They are totally against the popular notion that it is impossible to have a periodic material with long-range fivefold rotational order. It was therefore a big surprise to discover some intermetallics with sharp Bragg peaks (implying long-range order) showing 5- (or 10) fold rotational symmetry. The resolution of this apparent paradox was that the materials had a long-range ordered lattice but were not periodic. They are characterized not only by one periodicity but also by two periodicities which are incommensurate to each other (quasiperiodic). Actually, the consequence of having two incommensurate periodicities has been known in the world of geometry. For instance, 2D space can be tiled in a space-filling way to yield global fivefold symmetry as Roger Penrose had shown in the early 1970s (Penrose, 1974). Mathematically, the explanation predated the discovery by 10 years, but it was thought to be an interesting abstract problem in mathematics, not a template for real materials. Because of the remarkable but strange and esoteric nature of the idea, the interpretation of the experimental discovery had strong opponents (notably Linus Pauling, who thought it could be explained by twin structures of periodic crystals). Mathematicians love quasicrystals and have developed a theory of 6D periodic crystallography, where 6D direct and reciprocal lattices can be projected back into 3D following specific rules to yield the aperiodic 3D lattice and the

observed pattern of Bragg peaks. But if you make 6D crystals of 6D atoms and project them back to 3D, many atoms could be too close to each other, which is not physical. This implies that there should be some local atomic distortion in these materials. There are two problems in applying 6D crystallography to 3D materials. The first is to construct the lattice and project it back to 3D to explain the observed patterns of Bragg peaks. The second problem is how to “decorate” thus create an aperiodic lattice with atoms. The “decoration” problem is far from solved in most cases. The existence of defects and the difficulty in decorating the lattice make this an interesting PDF problem since PDF is directly sensitive to the atomic packing rather than any long-range order. In fact, the early studies of quasicrystals by PDF and DDF using the synchrotron X-rays and anomalous X-ray scattering (Kofalt *et al.*, 1986) and pulsed neutron PDF (Nanao *et al.*, 1987) were the intellectual stepping stones that helped to take the method from the study of glasses and liquids to crystals and quasicrystals using synchrotron-based radiation sources. It was found that, in icosahedral  $\text{Pd}_{58.8}\text{U}_{20.6}\text{Si}_{20.6}$ , quasicrystal uranium atoms occupy the corner positions of the quasicrystalline unit cells (Kofalt *et al.*, 1987). Later studies confirmed that the quasiperiodicity is very well reflected in the PDF (Shen *et al.*, 1988; Hu *et al.*, 1992; He *et al.*, 1993).

Obtaining the PDF for quasicrystals is relatively straightforward and can be done even with in-house X-rays. The paper by Bruhne *et al.* (2005) provides a nice direct comparison of the quality of PDFs that can be obtained from synchrotron X-rays with high  $Q$ -space resolution (ID31 at ESRF), low  $Q$ -space resolution (RAPDF data from 6ID-D at APS), and intermediate resolution but low  $Q_{\text{max}}$  data collected on a laboratory source (Fig. 8.15). In the low- $r$  region where the data were fit, the RAPDF data gave the highest real-space resolution due to their high  $Q_{\text{max}}$  and low noise, closely followed by the ID31 data. The in-house data were surprisingly good, though lower resolution. In the high- $r$  region, the high  $Q$ -resolution ID31 data were clearly best since the RAPDF data fell off much more quickly in  $r$ , though as is often the case, in a region of the PDF that was not modeled.

However, solving the atomic structure of quasicrystals exactly is a prodigiously difficult problem. In most cases, traditional crystallographic approaches were used to determine the structure of some simple quasicrystals such as  $\text{YbCd}_{5.7}$  (De Boissieu *et al.*, 2007; Takakura *et al.*, 2007). But the PDF method was also successful using models created by hand, by building up shells of atoms starting from a core cluster, as illustrated in Fig. 8.16 (Bruhne *et al.*, 2003, 2005).

### 8.3. COMPETING INTERACTIONS IN COMPLEX OXIDES

As we mentioned in Chapter 1, in many modern functional materials, responses to external stimuli are maximized by the use of competing interactions, which result in complex local structures. These local structures are quite

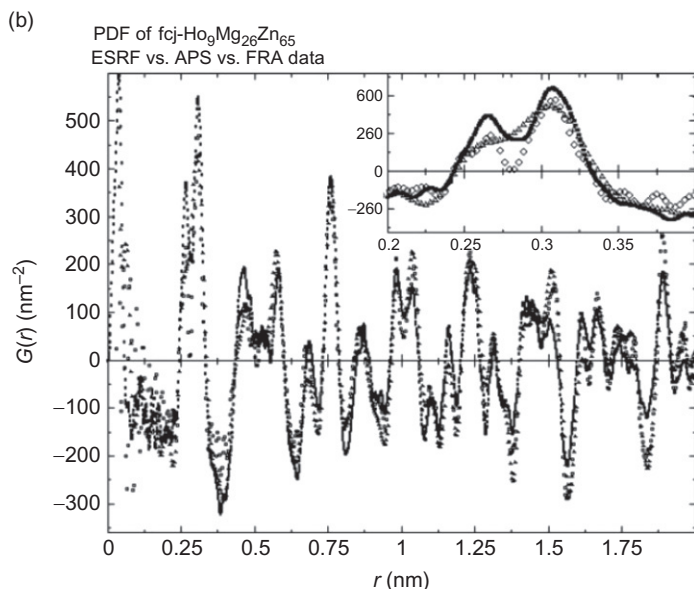


**FIGURE 8.15** PDFs from the quasicrystalline material  $\text{Ho}_9\text{Mg}_{26}\text{Zn}_{65}$ . There are three PDFs from the same material taken from three different diffractometers. The black symbols are from a RAPDF measurement with a  $Q_{\text{max}}$  of  $30 \text{ \AA}^{-1}$  measured at 6ID-D at the APS. The open symbols are from the ID31 diffractometer at ESRF with the same  $Q_{\text{max}}$  and the gray symbols are from an in-house diffractometer with a Mo  $K\alpha$  source and a  $Q_{\text{max}} = 13.5 \text{ \AA}^{-1}$  (Bruhne *et al.*, 2005).

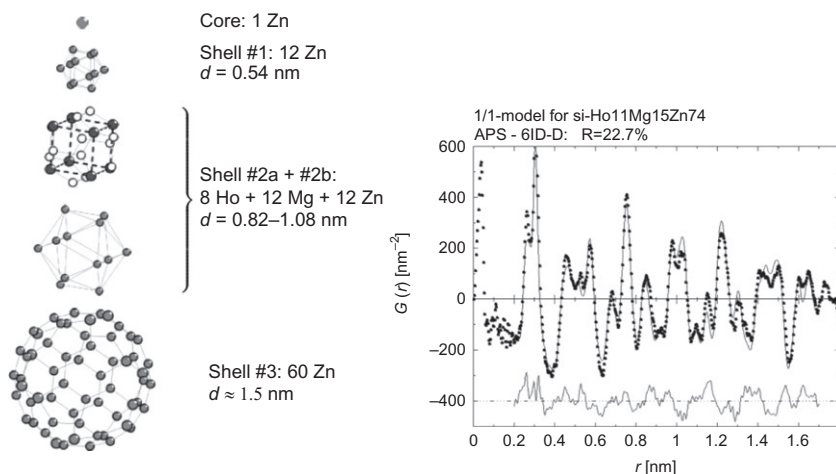


**FIGURE 8.16** Left: Structural models of the local structure of  $\text{Ho}_{11}\text{Mg}_{15}\text{Zn}_{74}$  built up from successive shells of atoms according to local rules. Right: The agreement of a calculated PDF from a periodic virtual approximant model of quasicrystal models shown on the left (Bruhne *et al.*, 2005).

often directly related to the desirable properties, making it important to study and understand them. The competing interactions produce complex internal structures primarily through a local feedback effect, as we see in this chapter. A secondary, but important, factor is the effect of disorder. The competing forces are quite often adjusted chemically, by alloying two or more constituent compounds. An example is the high-temperature superconductor  $\text{La}_{2-x}\text{Sr}_x\text{CuO}_4$  that is hole-doped by randomly replacing  $\text{La}^{3+}$  with  $\text{Sr}^{2+}$ . This alloying effect introduces atomic level chemical disorder. While this chemical disorder itself is usually unimportant, it triggers the competing forces to create complex local structures and pin local patterns so that the whole structure does not have the lattice periodicity (Dagotto, 2005). For this reason, these alloy solids are rich in complexity at various length scales, down to the nanometer scale, even when they appear to maintain long-range order in the structure. In this chapter, we discuss a number of representative cases that are of current interest.

### 8.3.1. PZT, $\text{Pb}(\text{Zr}_{1-x}\text{Ti}_x)\text{O}_3$

Replacing small amounts of Zr by Ti in the perovskite lead zirconate produces PZT,  $\text{Pb}(\text{Zr}_{1-x}\text{Ti}_x)\text{O}_3$ . This brings about dramatic changes in the structure and dielectric properties. While PZ is AFE, PZT is strongly FE for  $x > 0.05$ , and the symmetry of the structure changes from orthorhombic to rhombohedral (Jaffe *et al.*, 1971). PZT is widely used as a FE or piezoelectric material, in various applications, typically in actuators and sensors. It is often assumed that Ti drives the system to ferroelectricity, since Ti is more ferroelectrically polarizing. However, it is rather surprising to see such a small amount of the additive Ti creating dramatic changes in the whole of the oxide structure and properties. For only 5% of Ti to drive the structure of PZT to ferroelectricity, PZ itself must have some tendency toward ferroelectricity. For instance,  $\text{SrTiO}_3$  (STO) has a high dielectric constant and is almost FE. This is understood as a case of quantum paraelectricity in which the weak ferroelectricity is suppressed because of the diverging zero-point oscillations (Samara, 1971). Adding a small amount of FE impurity to STO drives the system to ferroelectricity (Mitsui and Westphal, 1961). However, pure PZ is a strong AFE with the Neel temperature of 511 K. How can only 5% of Ti kill such strong AFE?

The pulsed neutron PDF gave a clear answer to this question. As shown in Fig. 8.17, the PDF of  $\text{Pb}(\text{Zr}_{0.9}\text{Ti}_{0.1})\text{O}_3$  (PZT 90/10) is very similar to the PDF of PZ in the range up to 5 Å, in spite of large differences in the average structure (Egami *et al.*, 1997b), reflecting the different long-range crystal structure of these materials. This implies that upon addition of Ti, the local structure of Zr does not change much, which is understandable since both Zr and Ti are 4+ ions, and replacing Zr by Ti does not change the Madelung energy too much. Instead, what Ti does is to change the way the local

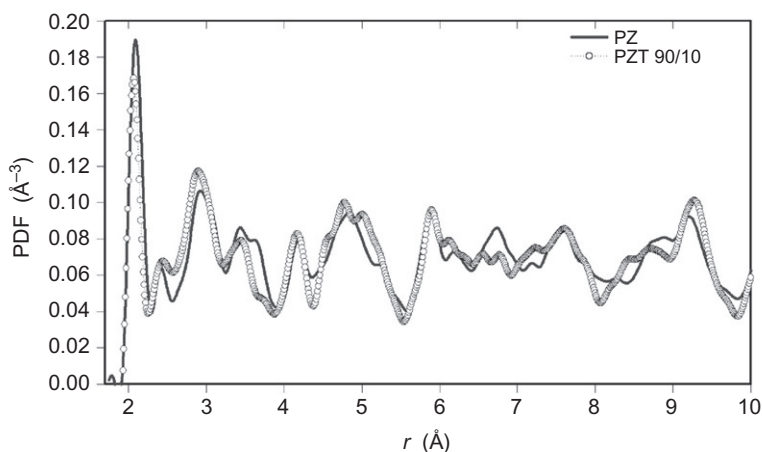


**FIGURE 8.17** PDF of PZ,  $\text{PbZrO}_3$ , compared to that of PZT(90/10),  $\text{Pb}(\text{Zr}_{0.9}\text{Ti}_{0.1})\text{O}_3$ . Note the similarity below  $r \sim 5$  Å despite the different average structures (orthorhombic and rhombohedral, respectively) (Egami *et al.*, 1997b).

structural units are arranged by altering the connectivity condition of the local units. The  $\text{ZrO}_6$  octahedra are rotated around the  $\langle 110 \rangle$  axes in PZ as mentioned above, while the  $\text{Ti}^{4+}$  ion is small and does not result in a local rotation. Consequently, Ti disrupts the connectivity of the local rotations so that the axis of rotation can change. Indeed, while the octahedra are rotated around  $\langle 111 \rangle$  in the rhombohedral phase of PZT according to the average structure, locally the rotation axis is still close to  $\langle 110 \rangle$  even in PZT (Teslic *et al.*, 1997). The direction of the rotation axis changes randomly at the Ti ion, for instance, from  $[110]$  to  $[101]$ , thus, on average, the rotation axis appears to be  $\langle 111 \rangle$ . Such a rearrangement of local units, actually, is most commonly observed during phase transformations in many oxide compounds, as we discuss below.

The change in the local rotation directly alters the AFE order. The origin of the AFE in PZ is the ionic size effect. Because  $\text{Zr}^{4+}$  ions are relatively large ( $0.72$  Å, Shannon, 1976), the tolerance factor of PZ is  $0.973$ . This leads to a buckling of the  $\text{Zr}-\text{O}-\text{Zr}$  bond and a rotation of the  $\text{ZrO}_6$  octahedra. Since rotation of one octahedron results in the rotation of the neighboring octahedra in the opposite sense, the rotation results in a doubling of the unit cell. In particular, it produces oxygen displacements with AFE order, which leads to the AFE ordering of the Pb polarization. This chain of rotations can be broken by a small cation such as  $\text{Ti}^{4+}$ . Furthermore, Pb polarization in PZ has FE fluctuations along the  $z$ -axis (Teslic and Egami, 1998). While the  $x$ - and  $y$ -polarizations have an AFE ordering, the  $z$ -axis polarization can develop ferroelectricity due to impurities such as  $\text{Ti}^{4+}$ . Thus, FE and AFE are not incompatible in complex systems and can locally coexist. The main

difference is that the long-range part of the AFE coupling is elastic in nature, while the FE is an electronic phenomenon associated with the long-range dipolar field and covalency.

### 8.3.2. Relaxor FE PMN, $\text{Pb}(\text{Mg}_{1/3}\text{Nb}_{2/3})\text{O}_3$

FE materials have strong dielectric and piezoelectric responses that are useful in various applications. However, the strong response is limited to the vicinity of the transition (Curie) temperature,  $T_C$ , and is strongly temperature dependent. This presents a major problem in devices. On the other hand, a class of materials called relaxor FEs show much milder temperature dependence and are very widely used technologically. Relaxor FEs show a diffuse, gradual FE transition and frequency-dependent dielectric response. The dependence of the dielectric response on frequency and temperature is very much like that of the mechanical or dielectric response of a glass, hence the origin of the name relaxor FE. The mechanism of relaxor ferroelectricity is obviously related to disorder, but its details are still controversial, as will be discussed below.

A prototypical relaxor FE is  $\text{Pb}(\text{Mg}_{1/3}\text{Nb}_{2/3})\text{O}_3$  (PMN). In this compound, the element of disorder is introduced by the occupation of the B-site by two ions with different valences ( $\text{Mg}^{2+}$  and  $\text{Nb}^{5+}$ ) and sizes (0.72 Å for  $\text{Mg}^{2+}$  and 0.64 Å for  $\text{Nb}^{5+}$ ). Interestingly, the initial explanation of relaxor behavior in PMN went in the opposite direction by invoking the presence of chemically ordered domains which result in charge imbalance (Husson *et al.*, 1988). However, this scenario has many problems. First of all, the charged domains of nanometer size would have a huge electrostatic energy. Second, this picture was developed to explain the relaxor behavior of heterovalent PMN, while the relaxor behavior is observed also in homovalent PZT when a small amount of Pb is replaced by La,  $(\text{Pb}_{1-x}\text{La}_x)(\text{Zr}_{1-y}\text{Ti}_y)\text{O}_3$  (PLZT), and this scenario cannot explain it. More importantly, recent work (Akbas and Davies, 1997) demonstrated in a very similar system,  $(\text{Pb}(\text{Mg}_{1/3}\text{Ta}_{2/3})\text{O}_3)_{0.9}(\text{PbZrO}_3)_{0.1}$  (PMT-PZ), relaxor behavior persists even when the chemical ordering extends to a macroscopic scale (micron-size). This proves finally that such nanodomains are irrelevant to the relaxor behavior. A crystallographic study of this system (Dmowski *et al.*, 2000) showed that the 1:1 ordering into the NaCl superlattice is made of  $\text{Ta}^{5+}$  in one sublattice and the other in the other sublattice, and macroscopically there is no charge imbalance.

The local structure of PMN determined by the pulsed neutron PDF method is very different from the PDF expected for the average crystal structure as shown in Fig. 8.18 (Egami *et al.*, 1991). Crystallographically, PMN has the structure of a nearly cubic simple perovskite, with a very slight rhombohedral distortion (note the rhombohedral distortion does not change the shape of the  $\text{BO}_6$  octahedron). However, the measured PDF reveals significant deviations of the local structure from the average structure. Not only are the PDF peaks broader, but there are peaks in the measured PDF that do not correspond to

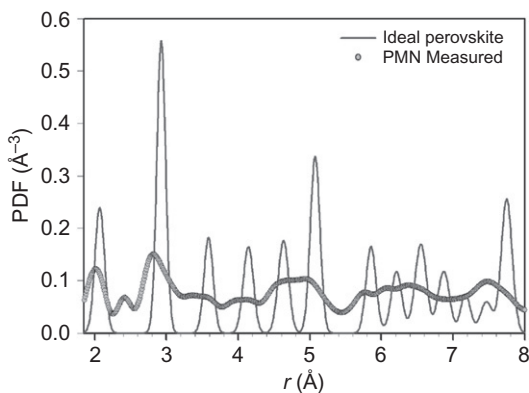


**FIGURE 8.18** Pulsed neutron PDF of PMN,  $\text{Pb}(\text{Mg}_{1/3}\text{Nb}_{2/3})\text{O}_3$ , compared to the PDF calculated for the ideal perovskite structure found crystallographically for PMN (Egami *et al.*, 1991).

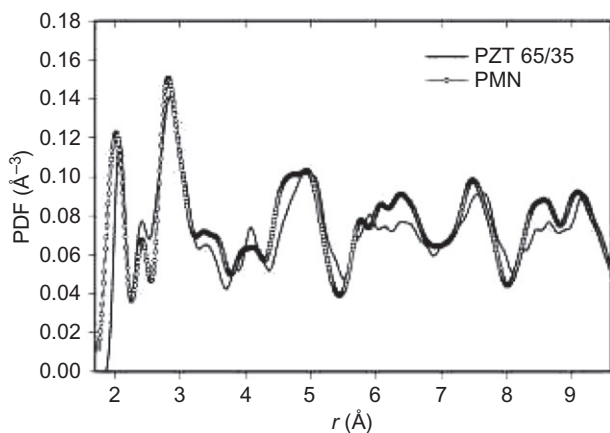


**FIGURE 8.19** PDF of PMN and PZT(65/35). Note the strong similarity despite the different average structures (Egami *et al.*, 1998).

the peaks in the perovskite PDF. In particular, there is a strong peak in the measured PDF at  $2.45 \text{ \AA}$ . The PDF of PMN is surprisingly similar to the PDF of PZT, as shown in Fig. 8.19, in spite of the difference in the average crystal structure. Both PZT and PMN feature the  $2.45 \text{ \AA}$  peak (Egami *et al.*, 1997a,b). Since the PDF of PZT is similar to the PDF of PZ as shown in Fig. 8.17, we can trace the origin of the  $2.45 \text{ \AA}$  peak to PZ and find that it is produced by the short Pb—O bonds due to lone-pair electrons. Thus, the peak at  $2.45 \text{ \AA}$  indicates the local polarization of the  $\text{PbO}_{12}$  cluster. This leads to an idea that a simple picture may describe the dielectric behavior of Pb containing perovskite-based FEs based upon the interacting  $\text{PbO}_{12}$  dipoles (Egami *et al.*, 1998).



### 8.3.3. Charge Ordering, Nanophase Separation, and Colossal Magnetoresistance in the Manganites

Magnetoresistance (MR) is the effect that the resistance changes when a magnetic field is applied. It is usually small in metals, with  $\Delta\rho/\rho$  of the order of 0.1–1%  $\text{T}^{-1}$ . Recently, metallic multilayered thin films such as Fe/Cr were found to show much larger MR ( $\Delta\rho/\rho \sim 0.1\text{--}0.5 \text{ T}^{-1}$ ) and the phenomenon was named “giant magnetoresistance” (Parkin, 1995). Since these films can modulate electric current by a magnetic field, they are also called “spin valves,” and are now widely used in magnetic recording heads and other devices. For the discovery of this effect, Grünberg and Fert were awarded 2007 Nobel Prize in physics. Manganites are complex oxides of manganese that can also show metallic behavior. Many of the manganite compounds  $(\text{R}_{1-x}\text{A}_x)_{n+1}\text{Mn}_n\text{O}_{3n+1}$  ( $\text{R} = \text{La, Pr, or Nd}$ ,  $\text{A} = \text{Sr, Ba, Ca, or Pb}$ ) are insulating in the paramagnetic phase but metallic in the ferromagnetic phase (Ramirez, 1997). Because of the coupling between the metallic behavior and the FE behavior, by applying a magnetic field and stabilizing the FE state, an insulator-to-metal transition can be induced. Since the magnitude of the change in resistance in terms of  $-\Delta\rho/\rho(H)$  can be as large as  $10^4$ , or 10<sup>6</sup>%, this phenomenon was coined “colossal magnetoresistance (CMR)” (Jin *et al.*, 1994).

The basic behaviors of the manganites were discovered already half a century ago (Jonker and Van Santen, 1950; Van Santen and Jonker, 1950), and the electronic mechanism to produce a ferromagnetic metallic phase was discussed by Zener (1951), Goodenough (1955), Hasegawa and Anderson (1955), and DeGennes (1960) in terms of the double-exchange (DE) mechanism. However, Millis *et al.* (1995) pointed out that the DE interaction is insufficient to explain the details of the CMR behavior. In particular, the DE model fails to explain the high electrical resistivity of the paramagnetic phase. They suggested that a strong electron–lattice interaction provides the missing resistivity via lattice-polaron formation. A lattice-polaron is a charge carrier that is trapped in the elastic deformation it created. In manganites, the polarons are directly related to the JT distortion. Various direct and indirect experimental methods have been mobilized to detect the polarons and successfully confirmed the presence of spin-lattice polarons. The PDF analysis played a major role in this process and also provided further insight into the physics of CMR (Billinge *et al.*, 1996; Louca *et al.*, 1997).

An even more recent realization has been that these materials are electronically microscopically (and sometimes macroscopically) inhomogeneous (Dagotto, 2005). PDF analysis had a role to play here too by identifying a coexistence of localized polaronic and delocalized metallic states coexisting over wide ranges of temperature and composition (Billinge *et al.*, 1996; Louca and Egami, 1999; Gutmann *et al.*, 2002; Bozin *et al.*, 2007, 2008).

In  $\text{La}_{1-x}\text{A}_x\text{MnO}_3$ , the replacement of trivalent La by a divalent ion such as  $\text{A} = \text{Ca, Sr, Ba, and Pb}$  reduces the effective valence of Mn or equivalently

introduces holes to the Mn—O bond. If the doped hole is localized on the  $\text{Mn}^{3+}$ , a JT ion, it becomes, at least nominally,  $\text{Mn}^{4+}$  (a non-JT ion). The exact state of the localized hole is an interesting problem by itself. With increased hole doping, the JT distortion in the average crystal structure quickly becomes smaller and disappears at about a doping level of  $x=0.17$ , and the structure becomes rhombohedral (Urushibara *et al.*, 1995). At 50% doping, many of the manganites, such as  $\text{La}_{1/2}\text{Ca}_{1/2}\text{MnO}_3$ , exhibit charge ordering and become insulating. When the doping exceeds 50%, the system remains a charge-ordered antiferromagnetic insulator.

In mixed-ion oxides such as  $\text{La}_{1-x}\text{A}_x\text{MnO}_3$  the local structure is expected to deviate from the average because of the ionic size difference between La and A. However, such deviations are only indirectly important for the CMR phenomenon. Local deviations that are central to the CMR phenomenon are those due to polaron formation. The local structure of this system was studied by the EXAFS method by several groups (Booth *et al.*, 1996; Tyson *et al.*, 1996; Lanzara *et al.*, 1998). More complete observations of local distortion due to polarons were made by using the pulsed neutron PDF method by Billinge *et al.* (1996) and Louca *et al.* (1997). Billinge *et al.* (1996) studied the variation of the pulsed neutron PDF with temperature for  $\text{La}_{1-x}\text{Ca}_x\text{MnO}_3$  and noted that the peak height at 2.75 Å changes anomalously with temperature as shown in Fig. 1.10. Below  $T_C$ , the height of this peak rises much more quickly with decreasing temperature for the samples with  $x=0.21$  and 0.25, than expected from the normal thermal effect. This peak in part includes the O—O distances in the  $\text{MnO}_6$  octahedra. Without the JT distortion, each octahedron has 12 O—O bonds that are 2.75 Å long, while with the JT distortion, 8 of them become 3.0 Å long. Consequently, the PDF peak height at 2.75 Å is reduced when there are local JT distortions. Thus, the results are consistent with having polarons involving JT distortions above  $T_C$  that disappear below  $T_C$ . This result confirmed the importance of the lattice in the CMR phenomenon and this has become one of the most highly cited PDF papers.

Direct evidence for this picture came from modeling the data. The changes in the local structure as the sample passes through  $T_C$  were observed by taking a difference between the PDFs measured just above and just below the transition. The structural changes are significant compared to the errors on the data as is evident in Fig. 6.6. These structural changes were well reproduced by a simple one-parameter model in which one-in-four sites, presumed to be the  $\text{Mn}^{4+}$  polaron sites, were distorted by an isotropic “breathing mode” collapse of 0.12 Å compared to the undistorted structure evident in the metallic phase. Because of the connectivity of the  $\text{MnO}_6$  octahedra, this distortion also results in a JT distortion appearing on the sites neighboring the  $4+$  site as illustrated in Fig. 8.20. Thus, in this model, the insulating phase is found to be made up of JT distorted  $\text{Mn}^{3+}$  sites and single-site  $\text{Mn}^{4+}$  polarons, whereas the ferromagnetic metallic phase is undistorted. The modeling was carried out at a doping level of  $x=0.25$  where the sample becomes significantly delocalized

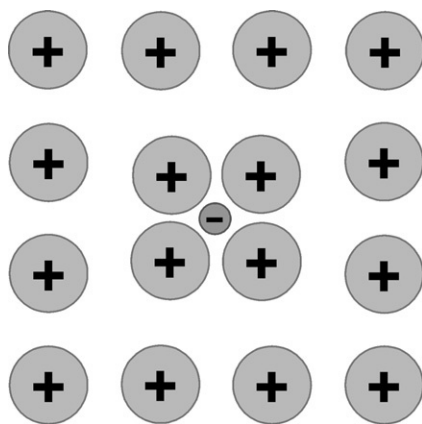


**FIGURE 8.20** Model of locally ordered polarons that polarize the Jahn–Teller distorted orbitals of neighboring octahedra. The size of the distortions is exaggerated for clarity (Billinge *et al.*, 2000).

at low temperature (Billinge *et al.*, 1996). As we discussed above, at lower levels of doping, the localized polaronic and delocalized metallic domains coexist even at low- $T$ . Nonetheless, the PDF provided direct structural evidence for the lattice-polarons involving JT distortions envisaged by Millis *et al.* (1995). The system has been studied using PDF over a wider range of doping where it is now evident that the size of the JT distortion decreases as the number of doped charges increases (Bozin *et al.*, 2007) even in the insulating phase. This is subtly different from the early understanding of single-site small polarons (Louca *et al.*, 1997; Louca and Egami, 1999) and implies that the polarons are forming nanosized domains that are larger than a single site. However, the main conclusion of the earlier study (Louca *et al.*, 1997; Louca and Egami, 1999) that the metal–insulator transition is inhomogeneous and dominated by percolation is still valid. The geometric modeling approach described in Chapter 6 was successfully applied to the modeling of locally correlated JT distorted octahedral in the undoped end-member (Sartbaeva *et al.*, 2007), but this modeling has not been extended to the doped region which would allow a more complete characterization of the inhomogeneous insulating phase of the manganites. However, at higher doping levels, the localized charges order, allowing them to be directly imaged in dark field transmission electron microscopy (Tao *et al.*, 2009, 2011) in the vicinity of 50%, confirming their presence and showing their size and distribution in space.

## 8.4. LOCAL CORRELATIONS AND PHASE TRANSITIONS

The subject of phase transitions is central to materials science and condensed-matter physics. This is partly because phase transitions bring about changes in

properties that are often drastic and sometimes useful, but also because the phenomenon itself is singular and fascinating. A good example is the FE phase transition. Below the FE Curie temperature,  $T_C$ , a FE crystal has an electric dipole moment and none above. Actually, even below  $T_C$ , a large crystal has no macroscopic polarization until an electric field is applied, since it has many FE domains with antiparallel polarizations. But within the domain, the solid is uniformly polarized. In terms of crystallography, a crystal is centrosymmetric above  $T_C$ , but loses centrosymmetry below. This transition represents a major qualitative change of the nature of the crystal.

Since phase transitions produce a change in the long-range order and macroscopic properties, they are usually studied from the global, long-range, point of view. For instance, the second-order phase transition is characterized by the correlation length diverging at the transition. The success of the renormalization group theory (Wilson, 1975) comes from making exact connections between the local interactions and the large length-scale fluctuations. Thus, it may appear that the PDF method that describes only the local correlations is not the right tool to study this phenomenon at all. However, as we will see below, PDF studies provide knowledge of important microscopic interactions that the measurement of the long-range order parameters cannot reveal. At the same time, we have to caution that it can cause unwanted confusion unless the results are interpreted correctly. For instance, the PDF method is an excellent technique to study ferroelectricity since a local polarization produces different cation–anion bond distances. This can be seen as a splitting of the metal–oxygen PDF peak in FE metal oxides. However, if one measures the PDF of such a material through the FE phase transition, the PDF often appears almost unchanged as shown in Fig. 8.21. What is going on? One interpretation, which is quite often made, is that the crystal retains the local atomic scale polarization even above  $T_C$ , and the phase transition is of the order–disorder type, which appears to be in conflict with the popular view that the FE phase transition occurs because of soft phonons, as explained below. How can we reconcile these two apparently opposing views? In order to resolve this conflict, we have to understand the dynamics and spatial correlation associated with the FE phase transition.

The first point to be considered is the dynamics of the phase transition and the phonon soft-mode. The FE soft-mode is the transverse optical (TO) mode in which cations are out of phase with anions. When the mode with  $q=0$  (infinite wavelength) becomes static, cations will be displaced in one direction while anions are displaced in the other resulting in long-range ferroelectricity. The mode becomes static when its frequency becomes zero and this is the origin of the name “soft-mode.” As the temperature is lowered toward the phase transition, the frequency of this particular  $q=0$  phonon mode gradually decreases (the “spring” softens) until it reaches zero at the phase transition. Soft-mode theory provides a very natural description of the FE transition.

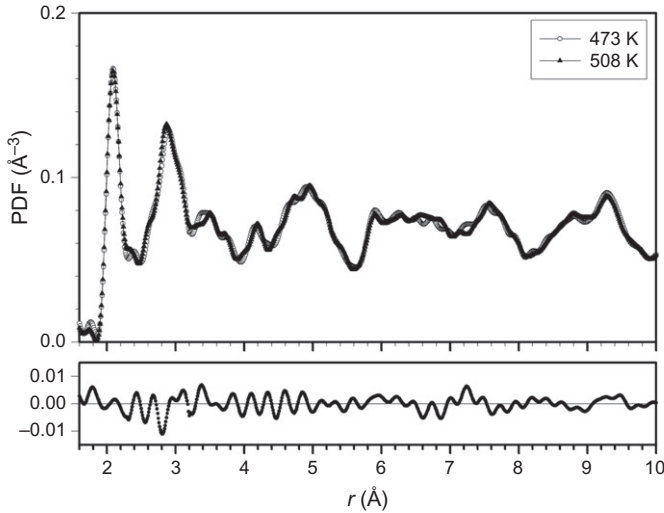


**FIGURE 8.21** Pulsed neutron PDF of PT at  $T=508$  and  $473$  K, above and below the ferroelectric phase transition temperature (above) and difference (below) (Teslic and Egami, 1998).

A more general description of second-order phase transitions is given by the Landau–Devonshire theory (Landau and Lifshitz, 1958; Salje, 1990; Gonzalo, 1991). In terms of the FE order parameter,  $\phi$ , the free energy near the phase transition can be expressed up to the fourth order in  $\phi$  as

$$G = G_0 + A\phi^2 + B\phi^4 + \dots \quad (8.1)$$

The free energy is minimized when  $\partial G / \partial \phi = 0$ , that is,

$$2A\phi + 4B\phi^3 = 0. \quad (8.2)$$

Thus,

$$\phi = \sqrt{\frac{-A}{2B}}. \quad (8.3)$$

The order parameter,  $\phi$ , is zero above the transition and finite below it, going continuously to zero at the transition. Thus, at  $T_C$ ,  $A=0$  and below  $T_C$ ,  $A < 0$ . In the mean-field approximation,  $A$  is linear with  $T$ :

$$A = A_0(T - T_C). \quad (8.4)$$

FE materials are piezoelectric so that the FE polarization is coupled to the elastic strain. The coupled system can then be described by

$$G = G_0 + A\phi^2 + B\phi^4 - \Gamma\phi\varepsilon + \frac{D}{2}\varepsilon^2, \quad (8.5)$$

where  $\varepsilon$  is the strain,  $\Gamma$  is the coupling constant, and  $D$  is the elastic constant. Elastic strain is a tensorial property, but for simplicity, it is presented as a scalar here. By minimizing  $G$  with respect to  $\varepsilon$ , we obtain

$$\phi = \frac{D}{\Gamma} \varepsilon. \quad (8.6)$$

Thus, Eq. (8.5) becomes

$$G = G_0 + D \left[ \frac{AD}{\Gamma^2} - \frac{1}{2} \right] \varepsilon^2 + \frac{BD^4}{\Gamma^2} \varepsilon^4. \quad (8.7)$$

which is minimum at

$$\varepsilon_0 = \frac{D}{\Gamma} \sqrt{\frac{A_0(T - T_C^*)}{2B}}, \quad T_C^* = T_C + \frac{\Gamma^2}{2A_0D} \quad (8.8)$$

indicating that the critical temperature is shifted from  $T_C$  to  $T_C^*$  due to the piezoelectric coupling. Expanding  $G$  around the minimum, we obtain

$$G = G_M + \frac{D^*}{2} d\varepsilon^2 + \dots, \quad D^* = \frac{2A_0D^2}{\Gamma^2} (T_C^* - T). \quad (8.9)$$

Thus, the effective, or renormalized, elastic constant,  $D^*$ , vanishes at  $T_C^*$ , and the phonon mode associated with polarization, usually the TO mode, becomes zero in energy.

As discussed in Chapter 7, the PDF measures the instantaneous structure which means we cannot tell directly from the PDF if some local correlations are static or dynamic in nature. Local displacements that become dynamic at the phase transition will thus persist in the PDF as long as they persist in the structure itself, which is why in FEs the atomic polarization appears to persist above  $T_C$ . Another point is that the correlation length of the FE polarization becomes longer as the temperature approaches  $T_C$ , so that from the local perspective long-range order appears to exist even when it is not static and infinite in range. For these reasons, from the viewpoint of the PDF, atomic polarizations appear to exist well above  $T_C$ . However, this is not inconsistent with the soft-mode theory. From the point of view of the critical phenomena, the dynamics of the PDF measurement is too fast, and the length scale too small, to capture the critical fluctuations near  $T_C$ . As we noted at the onset, the PDF method is not the method of choice if one tries to measure the critical fluctuations, though PDF method offers novel insights into the phase transition phenomenon in general in FEs, for example, as seen in the FE phase transition in  $\text{SrSnO}_3$  using RMC has been reported (Goodwin *et al.*, 2007).

## 8.4.1. Phase Transitions in Complex Materials

### 8.4.1.1. Hierarchy of Atomic Bonds

Since the strength of an atomic bond varies a lot from one species to another, in complex materials involving a large number of atoms, the atomic bonds

often have a natural hierarchy and organize themselves into groups of strongly bound atoms. For instance, in oxides, the bond between a metal and oxygen (M—O) is a strong covalent bond, while the metal–metal (M–M) interaction is weaker and ionic. The energy scale of the M—O bond is of the order of eV, thus too large to be influenced by thermal energy. Thus, the local unit, such as  $\text{BO}_6$  in the perovskites, behaves as a molecular unit. This is why the nearest-neighbor local structure in solids appears to change so little with temperature and often even through phase transitions. On the other hand, the energy scale of the interaction between these units is comparable to the thermal energy. What changes with temperature, therefore, is usually the second and third neighbor structure, determined by the interaction among the local units. Consequently, the order in the intermediate distances (3–10 Å) holds the key to understanding the properties. The PDF method has a unique strength in probing such distances, as has been demonstrated for the case of mixed FE oxides. The EXAFS method gives the distance to the nearest neighbor, but information about further neighbors quickly diminishes. Electron microscopy provides some information of the local structure, but only after averaging over the thickness of the sample.

#### 8.4.1.2. *Effect of Disorder*

In second-order transitions described by Eq. (8.1), the order parameter is spatially homogeneous and changes continuously as a function of temperature. However, elements of disorder, such as chemical compositional disorder due to alloying, tend to make the transition spatially inhomogeneous and diffuse. This is understandable since disorder produces the “local transition temperature” to be distributed, although a very small amount of disorder would not make a difference. The question is how much disorder the system can tolerate before the transition becomes diffuse. Depending on the strength and length scale of the disorder, either the critical fluctuations can smear the effect of disorder (weak disorder) or on the other hand the disorder can smear out the transition (strong disorder). The well-known Harris criterion states that the critical exponent of the specific heat is negative in the first case and positive in the second (Harris, 1974).

The PDF provides interesting insight on this problem. An example of the correlation smearing disorder is the case of mixed cations in FE systems resulting in the relaxor FE transition discussed above. For instance, relaxor behavior is observed in PZT when some Pb is replaced with La. As shown in Fig. 8.22, the PDF does not show marked changes even when the relaxor behavior sets in and ferroelectricity is destroyed. Replacing Zr with Ti already introduces disorder so that PZT is already strongly disordered. Additional disorder due to La brings about the relaxor behavior, which is why the amount of La necessary to induce the relaxor behavior decreases with the increasing Ti content. The mechanism of relaxor behavior is discussed below.

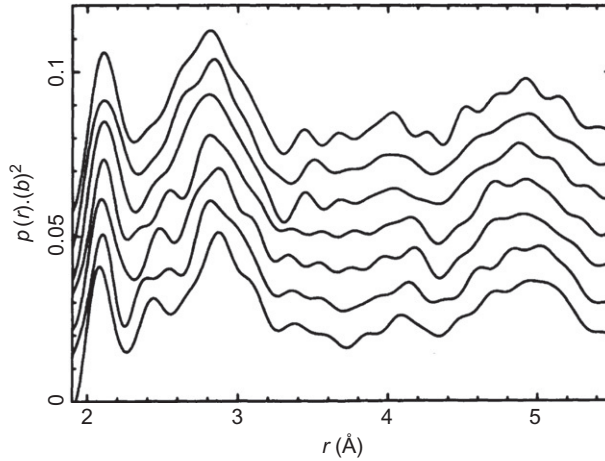


**FIGURE 8.22** PDF of PLZT,  $(\text{Pb}_{1-3/2x}\text{La}_x)(\text{Zr}_{1-y}\text{Ti}_y)\text{O}_3$ , for various La contents (Teslic *et al.*, 1996). Little change happens in the PDF even though the dielectric behavior changes markedly.

#### 8.4.1.3. Non-linearity and First-Order Transitions

Another factor that can destroy the second-order transition is a strong non-linearity of the interaction. A simple example is the theory of melting by Born (1939). While the applicability of this particular theory to this phenomenon is highly questionable (Tallon, 1984; Egami, 1997), it nicely illustrates the point. Let us consider the Hamiltonian of a harmonic oscillator with a higher order non-linear term,

$$H = \hbar\omega a^+a - \lambda a^+a^+aa, \quad (8.10)$$

where  $a$  and  $a^+$  are phonon annihilation and creation operators and  $\lambda > 0$ . The equation of motion for this system is

$$[a, H] = \hbar\omega a - 2\lambda a^+aa, \quad (8.11)$$

which, in the random-phase approximation, becomes

$$[a, H] = \hbar\omega a - 4\lambda \langle a^+a \rangle a = \hbar\omega' a, \quad (8.12)$$

where  $\omega'$  is the renormalized frequency. Thus, the phonon softening is proportional to the phonon density. Self-consistency requires

$$\langle a^+a \rangle = \frac{1}{e^{\hbar\omega'/kT} - 1}. \quad (8.13)$$

By solving these equations iteratively, the temperature dependence of the phonon frequency can be calculated. At a certain temperature, a catastrophic



softening takes place resulting in the first-order transition. There is a feedback mechanism in this system: the average phonon occupancy,  $\langle a^+a \rangle$ , increases as  $\omega'$  decreases (Eq. 8.13), but  $\omega'$  itself decreases with increasing  $\langle a^+a \rangle$  (Eq. 8.12). An easy way to see the catastrophic behavior at a critical value of  $\omega'$  is to use a high-temperature approximation for Eq. (8.13),

$$\langle a^+a \rangle \approx \frac{kT}{\hbar\omega'}. \quad (8.14)$$

Then from Eq. (8.12),

$$\omega' = \omega - \frac{4\lambda kT}{\hbar^2\omega'} \quad (8.15)$$

and

$$\omega' = \frac{\omega}{2} \pm \sqrt{\left(\frac{\omega}{2}\right)^2 - \frac{4\lambda kT}{\hbar^2}}. \quad (8.16)$$

The critical temperature is given by

$$T_C = \frac{\hbar^2\omega^2}{16k\lambda}, \quad (8.17)$$

where  $\omega'$  discontinuously jumps from  $\omega/2$  to zero.

First-order transitions result in a macroscopic or microscopic phase separation. Global properties such as conductivity are then determined by percolation of the different phases. It is possible to use the PDF analysis in a direct way to determine the state of microsegregation and the nature of the phase transition. For instance, the spatial correlation length of ionic displacements can be determined by modeling the PDF, up to about 30 Å at present, and possibly up to larger distances with greater computing power. In the homogeneous second-order transition, the correlation length diverges at the transition, while in disordered systems it remains finite and the transition occurs through percolation. An example is the metal–insulator transition in CMR oxides discussed below. Both theoretical and experimental evidences are accumulating supporting the idea of phase separation in certain cases.

### 8.4.2. Phase Transitions in Systems with Competing Interactions I: Relaxor Ferroelectricity

#### 8.4.2.1. Mechanism of Relaxor Ferroelectricity and the Origin of Spin-Glass Behavior

The phenomenon of relaxor ferroelectricity has many similarities to disordered magnetic systems, spin glasses in particular (Viehland *et al.*, 1992). Thus, we should first briefly review spin-glass behavior before discussing relaxor ferroelectricity. A spin glass is produced by three mechanisms, namely

random exchange, random field, and random anisotropy. In all cases, the second element with randomness is introduced which is in conflict with uniform ferromagnetism.

In a typical, “Heisenberg,” magnetic system, magnet and local spins interact via the Heisenberg exchange interaction

$$H = - \sum_{i,j} J_{ij} \mathbf{S}_i \cdot \mathbf{S}_j. \quad (8.18)$$

When  $J$  is uniformly positive ferromagnetism results, since parallel spins minimize the energy. But if the exchange interaction turns negative for a particular bond, it will disturb the local spin configuration. If enough local exchange interactions turn negative, the long-range ferromagnetic order becomes no longer stable, and the system collapses into a spin glass (Sherrington and Kirkpatrick, 1975). A typical phase diagram is shown in Fig. 8.23.

If a local field with random direction is applied on each spin, the Hamiltonian becomes

$$H = - \sum_{i,j} J_{ij} \mathbf{S}_i \cdot \mathbf{S}_j - \mu g \sum_i \mathbf{H}_i \cdot \mathbf{S}_i. \quad (8.19)$$

Imry and Ma (1975) have shown that for an order parameter with continuous symmetry (such as the Heisenberg magnet), the ordered state is unstable against any random field in dimensions less than four. The question is then how large the correlation is compared to the sample size. If the magnitude of the applied field is comparable to the exchange field, the direction of the spins varies strongly from site to site, resulting in the spin-glass state.

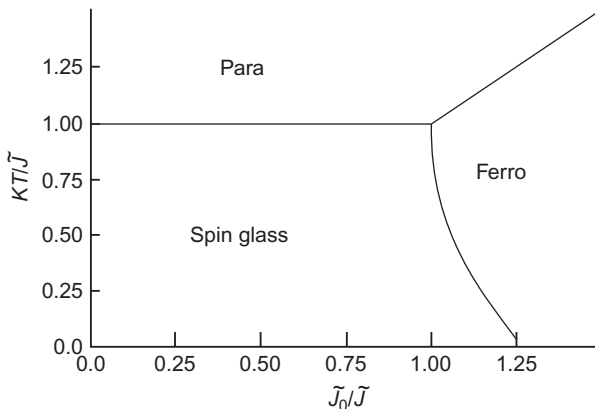


**FIGURE 8.23** The phase diagram of a spin-glass ferromagnet, an analogue for the mixed FE–AFE system (Sherrington and Kirkpatrick, 1975).

Spins interact with the lattice through the spin–orbit coupling and the crystal-field gradient. The lattice tries to orient the spin in a specific direction. Such a force can be described in terms of the local anisotropy energy,

$$E_a = - \sum_i \sum_{\ell, m} B_\ell^m Y_\ell^m(\mathbf{S}_i/S), \quad (8.20)$$

where  $Y_\ell^m(\mathbf{S}/S)$  are the spherical harmonics. If the local easy axis, along which the anisotropy energy is minimum, is not uniform, the collinear spin state is unstable. In this case as well ferromagnetism is unstable no matter how small the anisotropy is (Alben *et al.*, 1978; Pelcovits *et al.*, 1978). However, there is a fairly well-defined threshold below which the behavior is indistinguishable from a ferromagnet.

The total Hamiltonian, that is, the sum of the exchange Hamiltonian (Eq. 8.18) and the anisotropy energy (Eq. 8.20) may be further simplified by rotating the local axis in the direction of the easy spin polarization, and retaining only the  $\ell=2$ ,  $m=0$  term. The total Hamiltonian is called the Harris–Plischke–Zuckermann (HPZ) Hamiltonian (Harris *et al.*, 1973). The behavior of the system described by the HPZ Hamiltonian is now well understood. The critical parameter is the ratio between the average values of the Heisenberg exchange constant  $J_{ij}$  and the local parameter  $B(r_i)$ ,  $B/J$ . Theoretically, the system described by this Hamiltonian is always a spin glass; however, the magnetic correlation length  $\xi$  strongly depends upon the  $B/J$  ratio (Chi and Egami, 1979). Up to a critical value of  $B/J$ ,  $\xi$  is so large that the system behaves like a regular ferromagnet. As the value of  $B$  is increased, the system crosses over to a non-ergodic spin glass.

### 8.4.3. Mechanism of Relaxor Ferroelectricity

By analogy to spin glasses, ferroelectricity can be destroyed and a spin glass-like relaxor state can prevail if an element, or elements, that compete against ferroelectricity are introduced randomly with sufficient strength. We will first examine the dielectric equivalents of three mechanisms that destroy ferromagnetism.

#### 8.4.3.1. AFE Interaction

An AFE interaction usually originates from the rotation of the local units, such as  $\text{BO}_6$  tetrahedra. Because of connectivity through oxygen, the rotation of one  $\text{BO}_6$  in one sense induces the rotation of the neighboring  $\text{BO}_6$  in the opposite sense. This produces AFE of oxygen displacements, which usually induces an AFE displacement of A cations as well. The rotation of  $\text{BO}_6$  octahedra occurs because of the tolerance factor being less than unity. To accommodate small A-site ions,  $\text{BO}_6$  octahedra are rotated to reduce the B–B distance. Thus, AFE occurs for large B-site ions such as Zr. The

competition between the AFE and FE interactions can bring about the relaxor behavior (Chen *et al.*, 1996).

#### 8.4.3.2. Random Field

The local polarization can be tilted away from ferroelectricity by a local electric field. The most natural origin of the local field is the presence of heterogeneous ions, such as  $\text{Nb}^{5+}$  and  $\text{Mg}^{2+}$  in PMN. Theories based upon this idea were developed by Klemann and his associates (Westphal *et al.*, 1992). In their theory, the local variable is not the atomic level polarization, but the polarization in the polar nanodomain.

#### 8.4.3.3. Random Anisotropy

Random occupation of the B-site by different ions in PMN produces another local force equivalent to the local anisotropy that could produce the relaxor behavior (Egami, 1999). This is particularly applicable to the energetics of the local orientation of the Pb polarization. As shown in Chapter 10,  $\text{Pb}^{2+}$  ion is always strongly off-centered in the  $\text{PbO}_{12}$  cluster due to the lone-pair electrons, forming a strong local dipole. These dipoles are not free to rotate, since the off-centering of Pb in the  $\text{O}_{12}$  cage is produced by the displacement of oxygen ions rather than the displacement of Pb ions, thus the rotation and distortion of the  $\text{BO}_6$  octahedra are intimately connected to the Pb polarization. Consequently, the Pb dipoles can interact elastically through these B-site ions. Also, the compositional make-up of the B-site around Pb and the configuration of the  $\text{BO}_6$  octahedra determine the most likely direction of the Pb polarization. The magnitude of the dipolar moment is estimated to be  $p = 1.6 \times 10^{-19} \text{ C } \text{\AA}$ , corresponding to a very significant polarization of  $P = 0.22 \text{ C/m}^2$ , even assuming a Pb valence of +2. The value of  $p$  will be larger if we use the correct Born effective charge.

The local moments,  $p$ , interact with each other via various fields. We may describe this system by an effective Hamiltonian,

$$H_c = \sum_{i,j} J(\mathbf{r}_{ij}) \sum_{\ell,m} Q_\ell^m(\mathbf{P}_i) Q_\ell^{-m}(\mathbf{P}_j), \quad (8.21)$$

where  $\mathbf{P}_i$  is the local polarization of the  $i$ th Pb ion,  $Q_\ell^m(\mathbf{P}_i)$  are the spherical harmonic equivalents of  $\mathbf{P}_i$ , for instance  $Q_2^0(P) = 1/2[3P_z^2 - P^2]$ , etc. The  $\ell = 1$  term describes the pseudo-dipolar interaction due to the electric dipolar fields and hybridization fields through ferroelectrically active B-site elements. The  $\ell = 2$  term corresponds to the quadrupolar interaction due to strain fields. The local dipolar moments interact also with the lattice, since the rotation of the local moments requires displacements of oxygen ions that are coupled to the B-site cations. This dipole–lattice interaction may be described by the local anisotropy Hamiltonian,

$$H_a = \sum_i B_\ell^m(\mathbf{r}_{ij}) Q_\ell^m(\mathbf{P}_i). \quad (8.22)$$

The  $\ell = 1$  term describes the local electric field, while the  $\ell = 2$  term does the steric or elastic field that tends to confine  $\mathbf{P}$  along one direction which may be called the easy axis. In PMN, each Pb ion has about 3  $\text{Mg}^{2+}$  neighbors and 5  $\text{Nb}^{5+}$  neighbors. The electric field due to these heterogeneous charges cannot be expressed by a single electric field such as Eq. (8.19), but requires a tensorial description of Eq. (8.22). The dielectric properties of the interacting Pb dipoles should be described by the total Hamiltonian which is the sum of Eqs. (8.21) and (8.22), which is equivalent to the HPZ Hamiltonian for spin glass discussed above.

#### 8.4.3.4. Dynamics of Relaxor FE Systems

##### 8.4.3.4.1. Phonons in Relaxor Systems

The FE transition is induced usually by the softening of the TO phonon mode at  $Q=0$ . However, in the relaxor systems, because of the strong chemical and structural disorder, phonons are strongly scattered and have a short lifetime. In particular, phonons at low  $Q$  values are so strongly damped that they become invisible to neutrons, resulting in the “waterfall” phenomena (Gehring *et al.*, 2001; Wakimoto *et al.*, 2002; Stock *et al.*, 2004). This is consistent with the glassy nature of the ferroelectricity in the relaxor systems and the lack of the long-range ordering. The phonons “lost” from the  $Q$ - $\omega$  space are not really lost, but are merely localized. They may be seen more clearly in real space by the DPDF method (Chapter 7). For instance for PMN, the waterfall occurs in the energy range of about 10 meV (Gehring *et al.*, 2001), close to the energy range where DPDF shows the start of the splitting as shown in Fig. 7.11 (Dmowski *et al.*, 2008).

##### 8.4.3.4.2. Polar Nanoregions

The absence of the  $Q=0$  soft-mode is consistent with the diffuse nature of the FE transition in the relaxor FEs. In regular FEs, a well-defined FE phase transition occurs where FE correlation diverges to form long-range order. In the relaxor systems, FE correlation never diverges, and FE correlation remains short range to form the FE domains called polar nanoregions, PNR (Cross, 1987). The formation of PNR can be observed by the PDF through the local piezoelectric distortion. Figure 8.24 shows the temperature dependence of two PDF peaks of PMN (Jeong *et al.*, 2005). Clearly, the local structure changes significantly around the Curie temperature,  $T_C=300$  K. By modeling the PDF below 16 Å, it was found that the structure below 300 K is best described by the mixture of the cubic and rhombohedral phases. The rhombohedral distortion is consistent with the piezoelectric distortion due to the local polarization along [111] direction within the NPR. Indeed, the fraction of the

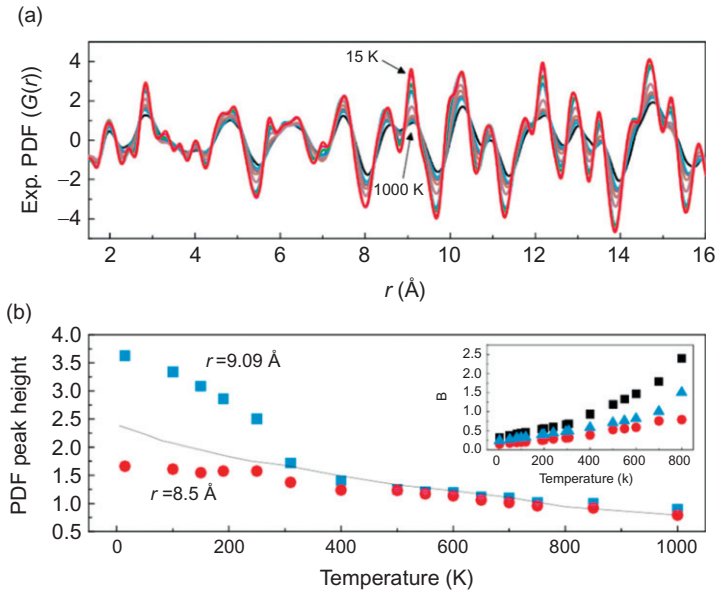


**FIG. 8.24** Temperature dependence of the PDF,  $G(r)$ , of PMN at  $T=15, 100, 190, 250, 313, 500, 650, 750$ , and  $1000$  K (a), and temperature dependence of the PDF peak height at  $r=8.5$  and  $9.09$  Å (b) (Jeong, *et al.*, 2005).

rhombohedral phase increases significantly below 300 K as shown in Fig. 8.25. It is most likely that the local rhombohedral distortion is a consequence of the formation of the NPR.

#### 8.4.3.4.2. Burns Temperature

Even though the FE response of PMN disappears above 300 K, its permittivity remains very high, making PMN useful for various applications. Moreover, optical refractive index shows anomalous temperature dependence up to 600 K suggesting strong dynamic polar fluctuations (Burns and Dacol, 1983). Such a behavior cannot be explained by the paraelectric response of atomic level polarization, such as local rattling of a Pb ion in the oxygen cage. It must mean that there are active regions of local collective polarization, such as PNR. Indeed, the DPDF integrated from 10 to 20 meV shows local dynamic polarization persisting up to about 600 K, seen as the satellite peak at  $2.4$  Å and the split peak at  $3.5$  Å (Fig. 7.13). In contrast, the static polarization, seen as the DPDF integrated from  $-5$  to  $5$  meV, disappears around 300 K (Fig. 7.12). Apparently, in addition to the conventional static PNRs, there are dynamic PNRs seen above the Curie temperature up to the Burns temperature. The static PNR is accompanied by piezoelectric lattice distortion, but the dynamic PNR is not. The

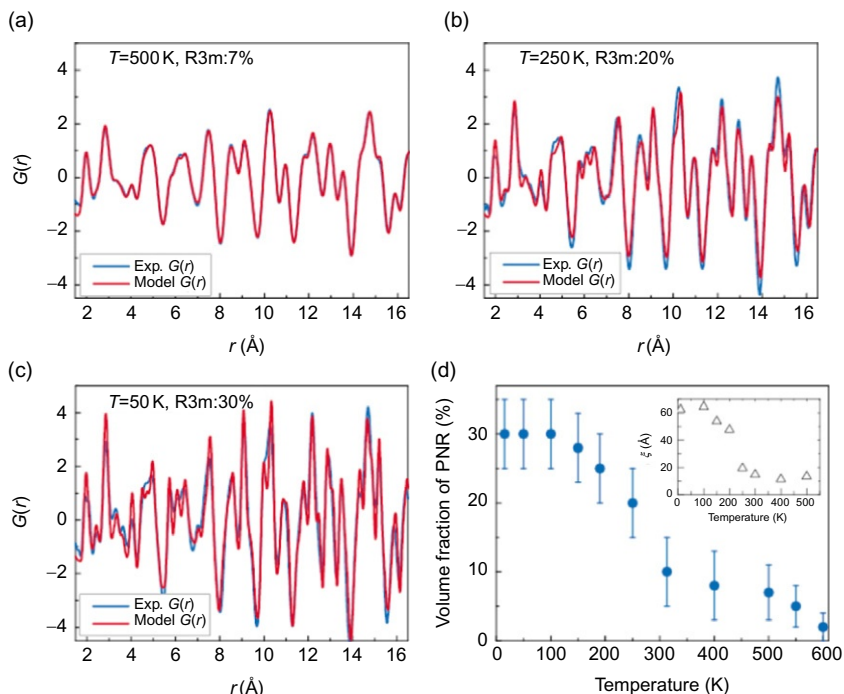


**FIGURE 8.25** Comparison of experimental PDFs with the PDFs calculated from a best-fit two-phase model that incorporates the polar nanoregions as a rhombohedral phase coexisting with a pseudo-cubic phase at (a)  $T=500$  K, (b)  $T=250$  K, and (c)  $T=50$  K. (d) The volume fraction of the rhombohedral polar nanoregion phase increases with decreasing temperature, reaching 30% at 15 K (Jeong *et al.*, 2005).

dynamic PNR could be characterized as the collective phonon cloud with polarization. However, the amplitude of Pb displacement in the dynamic PNR exceeds the regular phonon amplitude, typically  $0.1$  Å, and is similar to the magnitude of the static displacement below  $T_C$ , which is about  $0.25$  Å. Thus, the dynamic PNR represents indeed fluctuation of local FE polarization. Because of strong chemical and electrostatic disorder due to random placement of  $Mg^{2+}$  and  $Nb^{5+}$  ions, the FE correlation is prevented from becoming a long-range order and remains local dynamic correlation.

## 8.5. PHASE TRANSITION IN SYSTEMS WITH COMPETING INTERACTION: LITHIUM-NICKELATE

The structure and magnetism of  $LiNiO_2$  has been controversial, but a recent study using neutron PDF analysis all but closed the controversy. The

compound  $\text{LiNiO}_2$  has a layered structure, made of  $\text{NiO}_2$  layers and Li layers.  $\text{Ni}^{3+}$  ion is surrounded by six  $\text{O}^{2-}$  ions forming a  $\text{NiO}_6$  octahedron.  $\text{NiO}_6$  octahedra are connected by edge-sharing to form an  $\text{NiO}_2$  layer.  $\text{Ni}^{3+}$  ion has a  $d^7$  electron configuration, and the octahedral crystal-field splits it into the  $t_{2g}$  and  $e_g$  states. Because the crystal-field is dominant over the Hund's coupling,  $\text{Ni}^{3+}$  is in the low-spin configuration of  $t_{2g}^6$  and  $e_g^1$ . Since the  $e_g$  state is singly occupied,  $\text{Ni}^{3+}$  is JT active. Indeed, a sister compound,  $\text{NaNiO}_2$ , shows collective JT distortion with the Ni–O distance changing as much as 6% (Dyer *et al.*, 1954; Bongers and Enz, 1966). The mystery is that  $\text{LiNiO}_2$  does not show such a collective JT distortion, even though local JT distortion was observed by the EXAFS measurement (Rougier *et al.*, 1995; Nakai *et al.*, 1998). A part of complications is that Li–Ni site exchange happens, introducing disorder which could frustrate the long-range JT order. However, even when the site exchange is suppressed to the level of 2–3%, long-range JT order is not restored.

### 8.5.1. Hidden Phase Transition and Local Structure in $\text{LiNiO}_2$

The Rietveld analysis of the pulsed neutron diffraction data of  $\text{LiNiO}_2$  shows slight lattice distortion below  $T_d = 335$  K. Above  $T_d$ , the structure has the symmetry of  $R\bar{3}m$ , but below  $T_d$  the symmetry is lowered to  $C2/m$ , with the angle between  $[0, 0, 1]$  and  $[1, 1, 0]$  changing about  $0.15^\circ$  (Chung *et al.*, 2005). The distortion is very small, and at the same time, the diffraction peak  $[1, 0, 4]$  becomes wide, suggesting that this small distortion is merely a small part of the story.

The pulsed neutron PDF of  $\text{LiNiO}_2$  confirmed the observation by EXAFS that  $\text{NiO}_6$  octahedra are locally JT distorted (Chung *et al.*, 2005). The JT distortion is best seen by the first PDF peak due to Ni–O distances splitting into two subpeaks (Fig. 8.26b), just as the manganites shown in Fig. 8.27. Local JT distortions, however, are not collinear and form a trimer pattern, as determined by the PDF analysis, thus do not result in the macroscopic JT lattice distortion.

### 8.5.2. Domain Formation in $\text{LiNiO}_2$

Formation of a trimer pattern by the axes of the JT distortion explains the absence of the JT distortion in the lattice, but does not explain the observed phase transition. The capability of the PDF to describe the medium-range order solved this problem. The spectrometer used to collect the data on  $\text{LiNiO}_2$ , the NPDF of the Lujan Center of Los Alamos National Laboratory, has the  $Q$ -resolution of  $\Delta Q/Q = 0.0015$ . Thus, the PDF can be determined up to 300 Å. In most cases, the PDF is used to determine the local structure up to 10 or 20 Å as illustrated in this book. However, the PDF can be determined over a more extended range, and the case of  $\text{LiNiO}_2$  is an ideal example



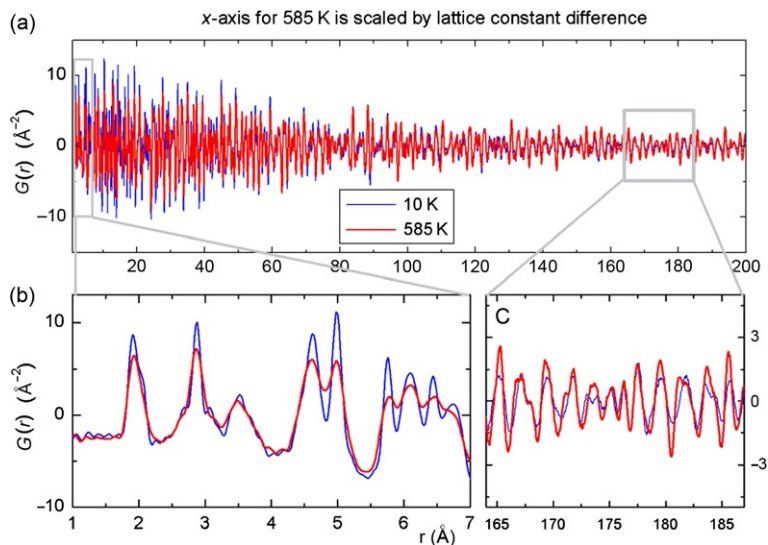


**FIGURE 8.26** (a) The PDF of  $\text{LiNiO}_2$  at 10 and 585 K. (b) The short-range part up to  $7 \text{\AA}$ . (c) The medium-range order from 165 to  $185 \text{\AA}$  (Chung *et al.*, 2005).

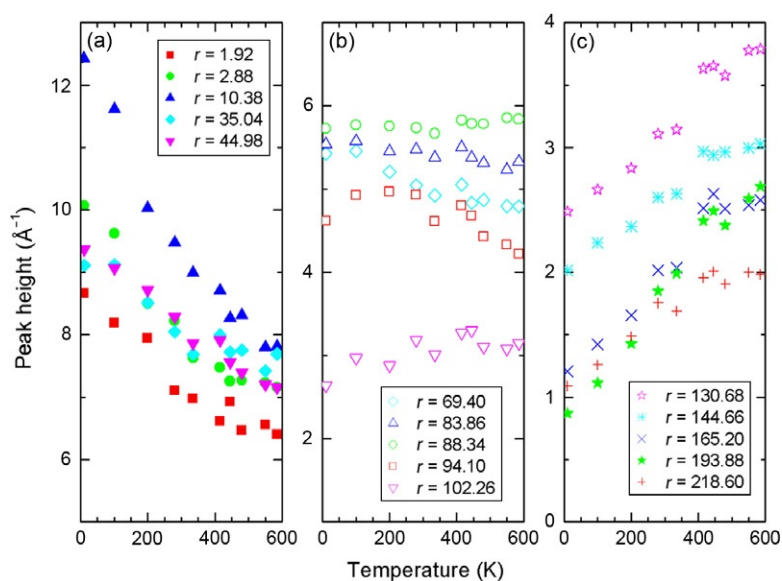


**FIGURE 8.27** Temperature dependence of the PDF peak heights of  $\text{LiNiO}_2$ .  $r$  indicates the peak position. (a) Up to  $50 \text{\AA}$ , (b) up to  $110 \text{\AA}$ , and (c) above (Chung *et al.*, 2005).

to demonstrate the power of the PDF to determine the medium-range order. As shown in Fig. 8.26a, the PDFs determined at 10 and 585 K are different, but in a strange way (Chung *et al.*, 2005). At short ranges, the PDF peak becomes less tall as temperature is raised because of phonon excitations, as shown in Figs. 8.26b and 8.27a. However, beyond about 90 Å, the temperature dependence becomes opposite; the PDF peak height increases with temperature as shown in Fig. 8.27c. This is because some domains with the size  $\xi_d \sim 90$  Å are formed below  $T_d$ . Inside the domain ( $r < \xi_d$ ), the PDF behaves regularly, with the peak height decreasing with increasing temperature because of phonons. However, at distances outside the domain ( $r > \xi_d$ ), the atomic correlation becomes weaker as domains are formed. The domains are formed because the trimer ordering of JT distortion cannot become long-range order. The JT axes which form the trimer pattern are not coplanar and tend to bend the plane as the order becomes extended. Thus, the local trimer order cannot grow into long-range order, but becomes limited to a nanodomain.

## REFERENCES

- Akbas, M. & Davies, P.K. (1997) *Commun. Am. Ceram. Soc.*, **80**, 2933.
- Alben, R., Becker, J.J. & Chi, M.C. (1978) *J. Appl. Phys.*, **49**, 1653.
- Billinge, S.J.L. (1992) PhD thesis, University of Pennsylvania.
- Billinge, S.J.L., DiFrancesco, R.G., Kwei, G.H., Neumeier, J.J. & Thompson, J.D. (1996) *Phys. Rev. Lett.*, **77**, 715.
- Billinge, S.J.L., Proffen, T., Petkov, V., Sarrao, J.L. & Kycia, S. (2000) *Phys. Rev. B*, **62**, 1203.
- Bongers, P.F. & Enz, U. (1966) *Solid State Commun.*, **4**, 153.
- Booth, C.H., Bridges, F., Snyder, G.J. & Geballe, T.H. (1996) *Phys. Rev. B*, **54**, R15606.
- Born, M. (1939) *J. Chem. Phys.*, **7**, 591.
- Bozin, E.S., Schmidt, M., DeConinck, A.J., Paglia, G., Mitchell, J.F., Chatterji, T., Radaelli, P.G., Proffen, T. & Billinge, S.J.L. (2007) *Phys. Rev. Lett.*, **98**(13), 4.
- Bozin, E.S., Sartbaeva, A., Zheng, H., Wells, S.A., Mitchell, J.F., Proffen, T., Thorpe, M.F. & Billinge, S.J.L. (2008) *J. Phys. Chem. Solids*, **69**(9), 2146–2150.
- Bruhne, S., Uhrig, E., Gross, C. & Assmus, W. (2003) *Cryst. Res. Technol.*, **38**, 1023.
- Bruhne, S., Uhrig, E., Luther, K.D., Assmus, W., Brunelli, M., Masadeh, A.S. & Billinge, S.J.L. (2005) *Z. Kristallogr.*, **220**, 962.
- Burns, G. & Dacol, F.H. (1983) *Solid State Commun.*, **48**, 853.
- Cao, D., Bridges, F., Kowach, G.R. & Ramirez, A.P. (2002) *Phys. Rev. Lett.*, **89**, 215902.
- Chapman, K.W., Chupas, P.J. & Kepert, C.J. (2005) *J. Am. Chem. Soc.*, **127**, 15630.
- Chen, I.-W., Li, P. & Wang, Y. (1996) *J. Phys. Chem. Solids*, **57**, 1525.
- Chi, M.C. & Egami, T. (1979) *J. Appl. Phys.*, **50**, 1651.
- Chung, J.-H., Proffen, Th., Shamoto, S.-I., Ghorayeb, A.M., Croguennec, L., Tian, W., Sales, B.C., Jin, R., Mandrus, D. & Egami, T. (2005) *Phys. Rev. B*, **71**, 064410.
- Cohen, W.E. (1992) *Nature*, **358**, 136.
- Comes, R., Lambert, M. & Guinier, A. (1968) *Solid State Commun.*, **6**, 715.
- Comes, R., Lambert, M. & Guinier, A. (1970) *Acta Crystallogr. A*, **26**, 244.
- Conterio, M.J., Goodwin, A.L., Tucker, M.G., Keen, D.A., Dove, M.T., Peters, L. & Evans, J.S.O. (2008) *J. Phys. Condens. Matter*, **20**, 255225.

- Cross, L.E. (1987) *Ferroelectrics*, **76**, 241.
- Dagotto, E. (2005) *Science*, **309**(5732), 257–262.
- De Boissieu, M., Takakura, H., Gomez, C.P., Yamamoto, A. & Tsai, A.P. (2007) *Philos. Mag.*, **87** (18–21), 2613.
- DeGennes, P.G. (1960) *Phys. Rev.*, **118**, 141.
- Dmowski, W., Akbas, M.K., Davies, P.K. & Egami, T. (2000) *J. Phys. Chem. Solids*, **61**, 229.
- Dmowski, W., Akbas, M.K., Egami, T. & Davies, P.K. (2002) *J. Phys. Chem. Solids*, **63**, 15.
- Dmowski, W., Vakhrushev, S.B., Jeong, I.-K., Hehlen, M.P., Trouw, F. & Egami, T. (2008) *Phys. Rev. Lett.*, **100**, 137602.
- Dyer, L.D., Borie, B.S.Jr., & Smith, G.P. (1954) *J. Am. Chem. Soc.*, **76**, 1499.
- Egami, T. (1997) *Mater. Sci. Eng. A*, **226–228**, 261.
- Egami, T. (1999) *Ferroelectrics*, **222**, 163.
- Egami, T., Rosenfeld, H.D., Toby, B.H. & Bhalla, A. (1991) *Ferroelectrics*, **120**, 11.
- Egami, T., Louca, D. & McQueeney, R.J. (1997a) *J. Supercond.*, **10**, 323.
- Egami, T., Teslic, S., Dmowski, W., Viehland, D. & Vakhrushev, S. (1997b) *Ferroelectrics*, **199**, 103.
- Egami, T., Dmowski, W., Akbas, M. & Davies, P.K. (1998) *AIP Conf. Proc.*, **436**, 1.
- Fujishita, H., Shiozaki, Y., Achiwa, N. & Sawaguchi, E. (1982) *Phys. Soc. Jpn.*, **51**, 3583.
- Gehring, P.M., Wakimoto, S., Ye, Z.-G. & Shirane, G. (2001) *Phys. Rev. Lett.*, **87**, 277601.
- Gonzalo, J.A. (1991) *Effective Field Approach to Phase Transitions and Some Applications to Ferroelectrics*. Singapore: World Scientific.
- Goodenough, J.B. (1955) *Phys. Rev.*, **100**, 564.
- Goodwin, A.L., Redfern, S.A.T., Dove, M.T., Keen, D.A. & Tucker, M.G. (2007) *Phys. Rev. B*, **76**(17), 11.
- Goodwin, A.L., Conterio, C.M., Dove, M.T., Evans, J.S.O., Keen, D.A., Peter, L. & Tucker, M.G. (2008) *Science*, **319**, 794.
- Gutmann, M., Bozin, E.S., Billinge, S.J.L., Babushkina, N.A., Belova, L.M., Kaul, A.R. & Gorbenko, O.Y. (2002) *Appl. Phys. A Mater. Sci. Process*, **74**, S892–S894.
- Harris, A.B. (1974) *J. Phys. C Solid State Phys.*, **7**, 1671.
- Harris, R., Plischke, M. & Zuckermann, M.I. (1973) *Phys. Rev. Lett.*, **31**, 160.
- Hasegawa, T. & Anderson, P.W. (1955) *Phys. Rev.*, **100**, 675.
- He, Y., Hu, R.J., Egami, T. & Shiflet, G.J. (1993) *Phys. Rev. Lett.*, **70**, 2411.
- Hu, R.Z., Egami, T., Tsai, A.P., Inoue, A. & Masutomo, T. (1992) *Phys. Rev. B*, **46**, 6105.
- Husson, E., Chubb, M. & Morell, A. (1988) *Mater. Res. Bull.*, **23**, 357.
- Imry, Y. & Ma, S.K. (1975) *Phys. Rev. Lett.*, **35**, 1399.
- Jaffe, B., Cook, W.R. & Jaffe, H. (1971) *Piezoelectric Ceramics*. London: Academic Press.
- Jeong, I.-K., Darling, T.W., Lee, J.K., Proffen, Th., Heffner, R.H., Park, J.S., Hong, K.S., Dmowski, W. & Egami, T. (2005) *Phys. Rev. Lett.*, **94**, 147602.
- Jin, T., Tiefel, H., McCormack, M., Fastnacht, R.A., Ramesh, R. & Chen, L.H. (1994) *Science*, **264**, 413.
- Jona, F. & Shirane, G. (1962) *Ferroelectric Crystals*. New York: Pergamon Press, Inc.
- Jona, F., Shirane, G., Mazzi, F. & Pepinsky, R. (1951) *Phys. Rev.*, **105**, 849.
- Jonker, G.H. & Van Santen, J.H. (1950) *Physica*, **16**, 337.
- Kofalt, D.D., Nano, S., Egami, T., Wong, K.M. & Poon, S.J. (1986) *Phys. Rev. Lett.*, **57**, 114.
- Kofalt, D.D., Morrison, I.A., Egami, T., Preische, S., Poon, S.J. & Steinhart, P.J. (1987) *Phys. Rev. B*, **35**, 4489.
- Kwei, G.H., Lawson, A.C., Billinge, S.J.L. & Cheong, S.-W. (1993) *J. Phys. Chem.*, **97**, 2368.
- Kwei, G.H., Billinge, S.J.L., Cheong, S.-W. & Saxton, J.G. (1995) *Ferroelectrics*, **164**, 57.
- Landau, L.D. & Lifshitz, E.M. (1958) *Statistical Physics*. Reading, MA: Addison-Wesley.

- Lanzara, A., Saini, N.L., Brunelli, M., Natali, F., Bianconi, A., Radaelli, P.G. & Cheong, S.-W. (1998) *Phys. Rev. Lett.*, **81**, 878.
- Lebedev, O.I., Van Tendeloo, G., Amelinckx, S., Leibold, B. & Habermeier, H.-U. (1998) *Phys. Rev. B*, **58**, 8065.
- Louca, D. & Egami, T. (1999) *Phys. Rev. B*, **59**, 6193.
- Louca, D., Egami, T., Brosha, E.L., Röder, H. & Bishop, A.R. (1997) *Phys. Rev. B*, **56**, R8475.
- Louca, D., Brosha, E.L. & Egami, T. (2000) *Phys. Rev. B*, **61**, 1351.
- Millis, A.J., Littlewood, P.B. & Shairman, B.I. (1995) *Phys. Rev. Lett.*, **74**, 5144.
- Mitchell, J.F., Argyriou, D.N., Potter, C.D., Hinks, D.G., Jorgensen, J.D. & Bader, S.D. (1996) *Phys. Rev. B*, **54**, 6172.
- Mitsui, T. & Westphal, W.B. (1961) *Phys. Rev.*, **124**, 1354.
- Nakai, I., Takahashi, K., Shiraishi, Y., Nakagome, T. & Nishikawa, F. (1998) *J. Solid State Chem.*, **140**, 145.
- Nanao, S., Dmowski, W., Egami, T., Richardson, J. & Jorgensen, J.D. (1987) *Phys. Rev. B*, **35**, 435.
- Parkin, S.P.P. (1995) *Annu. Rev. Mater. Sci.*, **25**, 357.
- Pelcovits, R.A., Pytte, E. & Rudnick, J. (1978) *Phys. Rev. Lett.*, **40**, 476.
- Penrose, R. (1974) *Bull. Inst. Math. Appl.*, **10**, 266.
- Proffen, T., DiFrancesco, R.G., Billinge, S.J.L., Brosha, E.L. & Kwei, G.H. (1999) *Phys. Rev. B*, **60**, 9973.
- Ramirez, A.P. (1997) *J. Phys. Condens. Matter*, **9**, 8171.
- Rodriguez-Carvajal, J., Hennion, M., Moussa, F. & Moudden, A.H. (1998) *Phys. Rev. B*, **57**, R3189.
- Rougier, A., Delmas, C. & Chadwick, A.V. (1995) *Solid State Commun.*, **94**, 123.
- Salje, E.K.H. (1990) *Phase Transitions in Ferroelastic and Co-elastic Crystals*. Cambridge: Cambridge University Press.
- Samara, G.A. (1971) *Phys. Rev. Lett.*, **27**, 103.
- Sartbaeva, A., Wells, S.A., Thorpe, M.F., Bozin, E.S. & Billinge, S.J.L. (2007) *Phys. Rev. Lett.*, **99**(15), 4.
- Shannon, R.D. (1976) *Acta Crystallogr. A*, **32**, 751.
- Shannon, R.D. & Prewitt, C.T. (1969) *Mater. Res. Bull.*, **4**(1), 57.
- Shechtman, D., Blech, I., Gratias, D. & Cahn, J. (1984) *Phys. Rev. Lett.*, **53**, 1951.
- Shen, Y., Dmowski, W., Egami, T., Poon, S.J. & Shiflet, G.J. (1988) *Phys. Rev. B*, **37**, 1146.
- Sherrington, D. & Kirkpatrick, S. (1975) *Phys. Rev. Lett.*, **35**, 1792.
- Singh, D. (1995) *Phys. Rev. B*, **52**, 12559.
- Stern, E.A. & Yacoby, Y. (1996) *J. Phys. Chem. Solids*, **57**, 1449.
- Stock, C., Birgeneau, R.J., Wakimoto, S., Gardner, J.S., Chen, W., Ye, Z.-G. & Shirane, G. (2004) *Phys. Rev. B*, **69**, 94104.
- Takakura, H., Gomez, C.P., Yamamoto, A., De Boissieu, M. & Tsai, A.P. (2007) *Nat. Mater.*, **6**(1), 58.
- Tallon, J.L. (1984) *J. Phys. Chem. Solids*, **41**, 837.
- Tao, J., Niebieskikwiat, D., Varela, M., Luo, W., Schofield, M.A., Zhu, Y., Salamon, M.B., Zuo, J.M., Pantelides, S.T. & Pennycook, S.J. (2009) *Phys. Rev. Lett.*, **103**(9), 097202.
- Tao, J., Niebieskikwiat, D., Jie, Q., Schofield, M.A., Wu, L.J., Li, Q. & Zhu, Y.M. (2011) *Proc. Natl. Acad. Sci. U.S.A.*, **108**(52), 20941–20946.
- Teslic, S. & Egami, T. (1998) *Acta Crystallogr. B*, **54**, 750.
- Teslic, S., Egami, T. & Viehland, D. (1997) *Ferroelectrics*, **194**, 271.

- Teslic, S., Egami, T. & Viehland, D. (1996) *The Journal of physics and chemistry of solids*, **57**, 1537.
- Tucker, M.G., Dove, M.T. & Keen, D.A. (2000) *J. Phys. Condens. Matter*, **12**, L723.
- Tucker, M.G., Keen, D.A. & Dove, M.T. (2001a) *Mineral. Mag.*, **65**, 489.
- Tucker, M.G., Squires, M.D., Dove, M.T. & Keen, D.A. (2001b) *J. Phys. Condens. Matter*, **13**, 403.
- Tucker, M.G., Dove, M.T. & Keen, D.A. (2002) S.J.L. Billinge & M.F. Thorpe (Eds.), *From Semiconductors to Proteins: Beyond the Average Structure* (p. 85). New York: Kluwer/Plenum.
- Tucker, M.G., Goodwin, A.L., Dove, M.T., Keen, D.A., Wells, S.A. & Evans, J.S.O. (2005) *Phys. Rev. Lett.*, **95**, 255501.
- Tyson, T.A., Mustre de Leon, J., Conradson, S.D., Bishop, A.R., Neumeier, J.J. & Zang, J. (1996) *Phys. Rev. B*, **53**, 13985.
- Urushibara, A., Moritomo, Y., Arima, T., Asamitsu, A., Kido, G. & Tokura, Y. (1995) *Phys. Rev. B*, **51**, 14103.
- Van Santen, J.H. & Jonker, G.H. (1950) *Physica*, **16**, 599.
- Viehland, D., Li, J.E., Jang, S.J., Cross, L.E. & Wuttig, M. (1992) *Phys. Rev. B*, **46**, 8013.
- Wakimoto, S., Stock, C., Birgeneau, R.J., Ye, Z.-G., Chen, W., Buyers, W.J.L., Gehring, P.M. & Shirane, G. (2002) *Phys. Rev. B*, **65**, 172105.
- Westphal, V., Kleemann, W. & Glinchuk, M.D. (1992) *Phys. Rev. Lett.*, **68**, 847.
- Wilson, K. (1975) *Rev. Mod. Phys.*, **47**, 773.
- Woodward, P.M. (1997a) *Acta Crystallogr. B*, **53**, 32.
- Woodward, P.M. (1997b) *Acta Crystallogr. B*, **53**, 44.
- Zener, C. (1951) *Phys. Rev.*, **81**, 440.